Combining Astrometry and Photometry to Improve Orbit Retrieval of Directly Imaged Exoplanets

A thesis presented

by

Margaret Bruna

to

The Department of Physics

in partial fulfillment of the requirements

for the degree of a

Master's

in the subject of

Astronomy & Astrophysics

McGill University

Montréal, Québec

© 2022 — Margaret Bruna All rights reserved.

Combining Astrometry and Photometry to Improve Orbit Retrieval of Directly Imaged Exoplanets

Dissertation Advisor: Professor Nicolas Cowan

Abstract

Future missions like Roman, HabEx, and LUVOIR will directly image exoplanets in reflected light. While current near-infrared direct imaging searches are only sensitive to young, self-luminous planets whose brightness is independent of their orbital phase, reflected light imaging will reveal changes in planet brightness over the course of an orbit due to phase variations. One of the first objectives will be determining the planet's orbit via astrometry, the projected position of the planet with respect to its host star in the sky plane. We show that phase variations can significantly improve the accuracy and precision of orbital retrieval with two or three direct images. This would speed up the classification of exoplanets and improve the efficiency of subsequent spectroscopic characterization. We develop a forward model to generate synthetic observations of the two dimensional position of the planet with respect to its host star on the sky plane, and the planet/star flux ratio. Synthetic data are fitted with Keplerian orbits and Henyey-Greenstein phase variations to retrieve orbital and phase parameters. For astrometric uncertainties of 0.01 AU in projected separation and flux ratio uncertainties of 10^{-12} , using photometry in orbit retrieval improves the accuracy of semi-major axis by 47% for two epochs and 61% for three epochs if the phase curves have a known shape, but unknown amplitude. In the more realistic scenario where the shape and amplitude of the phase curve are a priori unknown, photometry still improves accuracy by 16% for two epochs and 50% for three.

Contents

Abstract						
\mathbf{A}	ckno	wledgr	nents	vii		
D	edica	ation		viii		
1	Intr	oducti	ion	1		
	1.1	Direct	Imaging	1		
	1.2	2.2 Current Direct Imaging Technology				
	1.3	Future	e Missions	5		
	1.4	Orbit	Retrieval	8		
	1.5	Nume	rical Methods	10		
		1.5.1	Bayesian Statistics	10		
		1.5.2	Markov chain Monte Carlo methods	12		
2			g Photometry and Astrometry to Improve Orbit Retriev y Imaged Exoplanets	al 15		
2.1		Introduction				
		2.1.1	Orbit retrieval via planetary astrometry	16		
		2.1.2	Phase variations for orbit retrieval	16		
	2.2	Metho	ods	17		
		2.2.1	Keplerian Orbits and Henyey-Greenstein Phase Curves	17		

CONTENTS

3	Cor	clusio	n	35
9	Cor	aludio.	~	25
		2.4.3	Conclusions	33
		2.4.2	Summary	33
		2.4.1	Caveats	32
	2.4	Discus	ssion	32
		2.3.2	Orbit retrievals for 2, 3, and 4 epochs	28
		2.3.1	Single epoch posterior on semi-major axis	24
	2.3	Result	ts	24
		2.2.3	Retrieving orbital and phase parameters	22
		2.2.2	Synthetic planets and observations	20

Acknowledgments

I would like to thank my supervisor Prof. Nicolas Cowan for giving me this project and taking me on as a grad student. I would also like to thank my fellow MEChA research group members for technical help but also for being my friends through such a socially isolating degree. In particular, I'd like to thank Lisa Dang for her support and reassurance during particularly difficult moments. I'd also like to thank Zoe Kearney, my office-mate, for being a great friend and listener. Thank you Ell Bogat, Samantha Hassler, Rhonda Morgan, and Chris Stark for valuable discussions at the 240th AAS Meeting and the StSci Spring 2021 Symposium, and for taking an interest in my work. Thank you Ben Farr for taking the time to help me with kombine, and Tyler Robinson for valuable help with fleshing out current and future ideas for research. Finally, I'd like to thank my partner Ben Merrell for always being grounding and endlessly supportive.



Chapter 1

Introduction

The first definitive detection of planets outside our solar system occurred in 1992 when two exoplanets were found by Wolszczan & Frail (1992) orbiting the pulsar PSR 1257+12. Since then 5044 exoplanets have been confirmed, and thousands more potential candidates have yet to be confirmed (NASA Exoplanet Science Institute Website 2020). The field of exoplanet research has boomed — there is no shortage of work to be done.

Although many exoplanets have been found, they are incredibly challenging to see because they are so small and dim compared to the stars they orbit. Most techniques employed to find exoplanets rely on indirect methods. As evidenced in Figure 1.1, the most fruitful has been the transit method: a star will dim periodically as a planet moves into our line of sight. The next most successful method is radial velocity: the gravitational pull of an orbiting planet causes a star to wobble, which changes the colour of starlight received by telescopes. Both methods are most sensitive to planets orbiting on shorter periods, close to their host star. These techniques have allowed us to obtain a very detailed understanding of the demographics of these short period planets. Figure 1.1 indicates a glaring dearth of long period planets that do not pass in front of their star very often and do not pull their star hard enough. Different planet detection techniques are needed to detect planets on long orbits.

1.1 Direct Imaging

Directly detecting a planet (taking a direct image) provides an excellent complement to the techniques mentioned above. Radial velocity can estimate a planet's mass.

Mass — Period Distribution

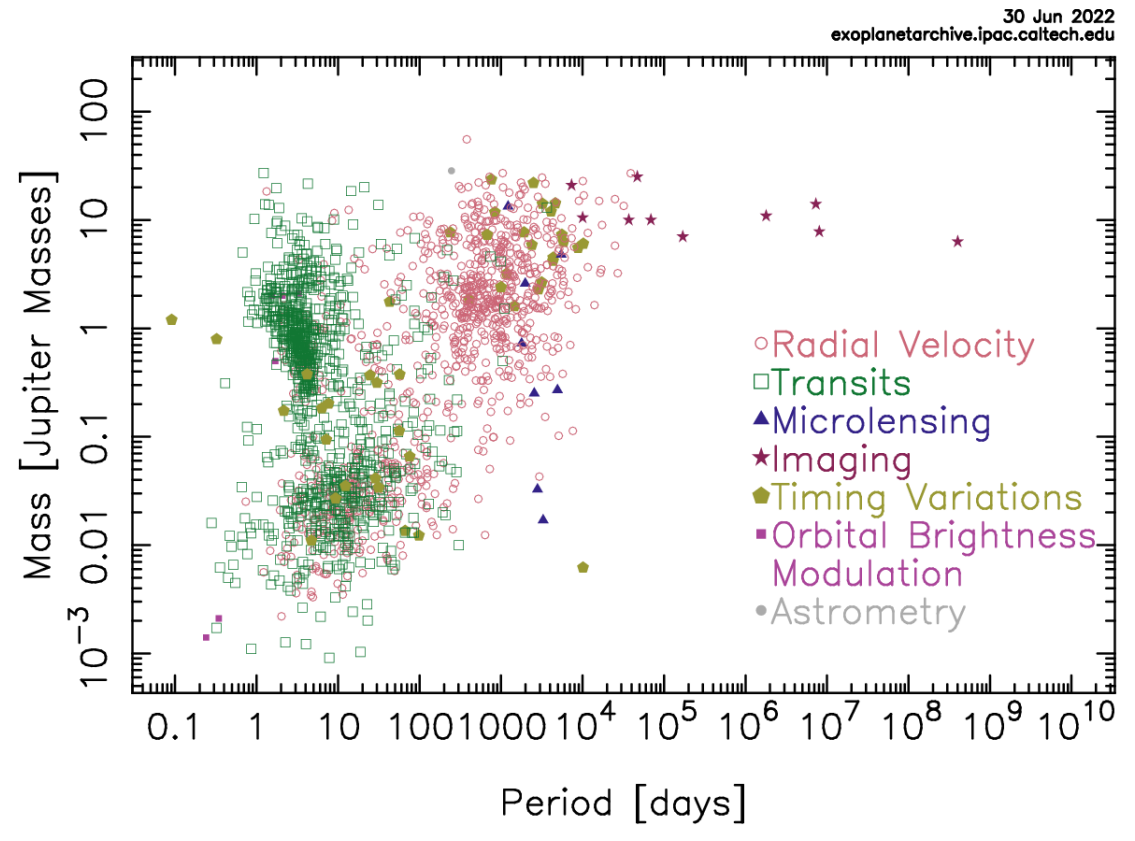


Figure 1.1: Exoplanet demographics by mass and period distributions, with axes on a log-scale. Each data point corresponds to a detection method. Notably, pink circles correspond to planets found via radial velocity. Green squares correspond to planets found via the transit method. Purple stars correspond to planets found via direct imaging. This plot was generated from data found on the NASA Exoplanet Science Institute Website (2020).

Transits reveal a planet's radius and orbital period. Transit spectroscopy can reveal information about a planet's atmosphere: starlight passing through the upper layer of the planet's atmosphere is imprinted by molecular absorption lines. However, this is limited to atmospheres with large scale heights, typically planets orbiting on very short periods.

Direct imaging is undoubtedly the future of exoplanet characterization. Directly detecting a planet provides a measurement of luminosity and probes atmosphere composition (Traub & Oppenheimer 2010). Additionally, determining a planet's location in the sky plane allows for orbit characterization. Though the scientific gains of direct imaging are valuable, in practice it is an incredible technological

feat. Stars are many orders of magnitude brighter than planets they host, making them hard to resolve. For a solar-system analog located at 10 pc, the brightest planet would be 10^{-9} times dimmer than the host star (in visible wavelengths) at a separation of 5 arcseconds (Fischer et al. 2014). The challenge lies in blocking out the light from the much bigger host star while still receiving light from the planet. Current direct imaging is done in infrared, where the planet/star flux ratio can be many orders of magnitude larger. Giant (1-2 Jupiter radii), young, and hot self-luminous planets are thus great targets for current direct imaging projects with contrast ratios of about $10^{-5} - 10^{-6}$ (Fischer et al. 2014).

1.2 Current Direct Imaging Technology

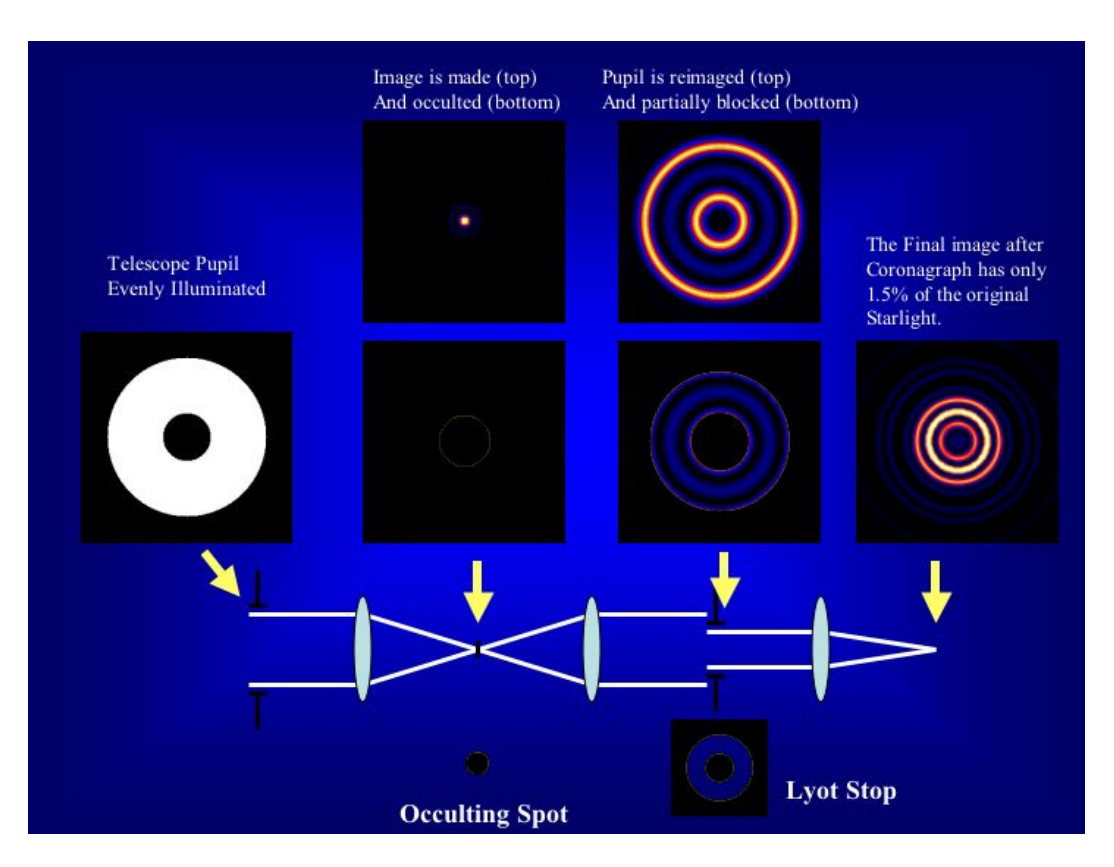


Figure 1.2: The basics of how a Lyot coronagraph works. Taken from the Lyot Project of the American Museum of Natural History (Oppenheimer 2003).

So far, direct imaging has primarily been done with ground-based telescopes. Planets are resolved by first blocking out starlight before image processing and using adaptive optics (AO) to correct for atmospheric turbulence and wavefront errors. Telescopes most commonly use a Lyot coronagraph to block starlight while

still receiving any surrounding light by using a series of lenses and filters, the principles of which are shown in Figure 1.2. These systems have a diffraction limit of $\approx 1.22 \lambda/D$, meaning improved performance requires larger telescope diameters and the capability of imaging at smaller wavelengths, both of which are expensive and technologically challenging. As mentioned previously, images are currently taken in near-infrared light (800 - 2500 nm) since planets are typically brighter and stars are typically dimmer in this wavelength - so the contrast between a planet and star is much less than in visible light (2×10^{-5} to 10^{-6} in the near-IR vs 10^{-8} in visible light for Jupiter-sized planets) (Macintosh et al. 2014; Spiegelhalter & Rice 2009). Imaging planets in near-IR means the inherent heat from the planet is being probed, making this technique most sensitive to young (very hot), giant, Jupiter sized planets. Direct imaging also favours planets that orbit far from their star, as demonstrated in Figure 1.1. This is due to the occulting disk of the coronagraph to block out starlight, and the fact that planets appear close to their star when imaged accross interstellar distances.

The first generation of instruments equipped with AO and near-IR imaging capabilities on ground-based facilities like the NaCo on the Very Large Telescope (VLT) and NIRI on Gemini have led to crucial discoveries in exoplanet imaging, like the first direct image of a planet-mass companion by Chauvin et al. (2004). The Gemini and Keck telescopes also led to the discovery of the HR8799 system by Marois et al. (2008, 2010), which is the only multi-planet system found using this technique. Figure 1.3 shows these four planets orbiting around their host star.

The Gemini Planet Imager (GPI) and the Spectro-Polarimetric High-contrast Exoplanet Research instrument (SPHERE) offer vast improvements over the first generation of planet imagers mentioned above. Both have had similar timelines and science goals. While very large and hot planets are easier to resolve than those that are smaller and older, achieving the necessary contrast ratios ($\sim 10^{-6}$) is still a technological challenge that these instruments have been built to overcome. SPHERE and GPI were designed to provide the best possible contrast ratio, achieving an order of magnitude improvement compared to their predecessors.

GPI was designed for the Gemini South telescope. It saw first light in 2013 by imaging Beta Pictoris b (Macintosh et al. 2014), which was first imaged by the NaCo instrument on the Very Large Telescope (VLT) by Lagrange et al. (2008). Between 2014 and 2018, GPI surveyed 532 stars for an hour each, obtaining deep spectra of 6 exoplanets (Macintosh 2021). SPHERE was designed for the European Southern Observatory's Very Large Telescope (VLT) and saw first light in 2014 (Beuzit et al. 2019). After four years of operations GPI and SPHERE have yielded 3 new detections of previously unknown exoplanets (Macintosh 2021). Though this is

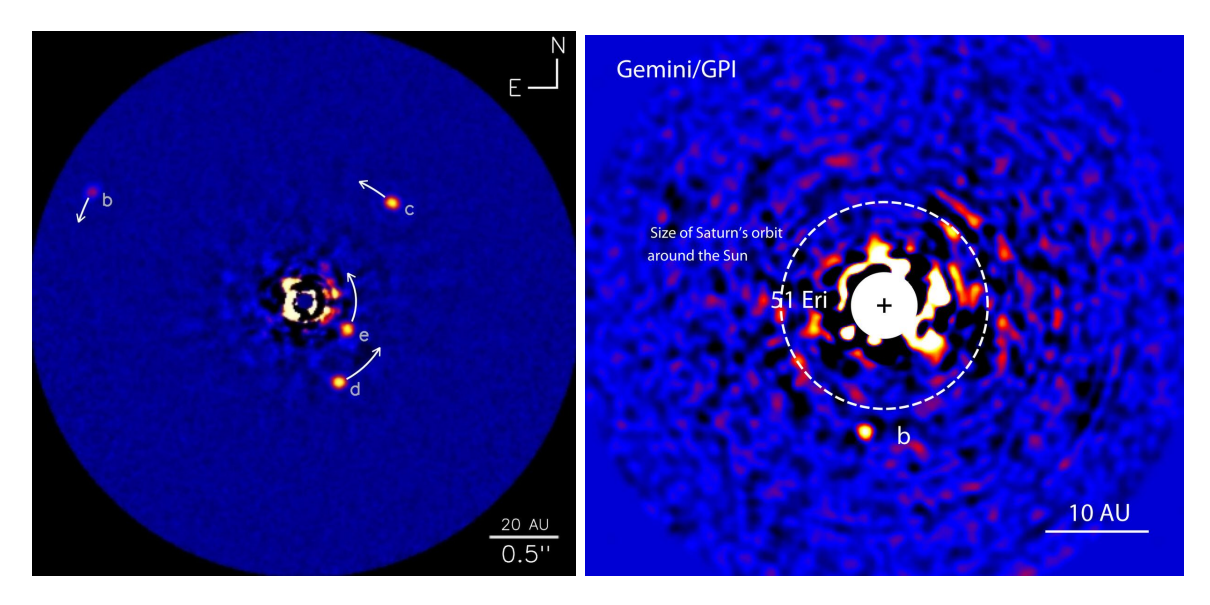


Figure 1.3: Left: Directly Imaged HR 8799 system, discovered by Marois et al. (2008, 2010) using the Keck telescope. Planets b, c, d, and e have semi-major axes of $\sim 68, 43, 27$, and 17 AU, respectively (Zurlo et al. 2016). Right: Directly imaged 51 Eridani b, which was discovered by Macintosh et al. (2014) using the Gemini Planet Imager, and has a semi-major axis of ~ 11 AU.

perhaps dishearteningly low, these surveys have helped to confirm that young giant sized planets orbiting at large distances are quite rare, which is in agreement with population synthesis models (Mordasini et al. 2017). Also, the first planet discovered with GPI by Macintosh et al. (2015), 51 Eridani b, sparked particular interest since it is the closest we have come to finding a young Jupiter analog and has thus been a milestone in informing how our own Jupiter may have formed.

1.3 Future Missions

Instruments like GPI and SPHERE have pushed the capabilities of ground based imaging and have provided the community with incomparable scientific knowledge. But the gap in exoplanet population demographics for longer period planets remains. Future ground based facilities in the 30 meter class are being built with the objective of filling in this gap in mind (among others). The Thirty Meter Telescope (TMT), the European Extremely Large Telescope (E-ELT), and the Giant Magellan Telescope (GMT), will have the angular resolution to directly image smaller planets $(R_{\oplus} < 4R_{\oplus})$ around nearby M-dwarf stars in the mid-IR (Crossfield 2013; Quanz et al. 2014; Bowens et al. 2021). These larger telescopes are predicted to have

the sensitivity and spatial resolution to image planets orbiting at separations of 1 astronomical unit (AU) away from their star (Chauvin 2018). Direct imaging with this class of extremely large ground-based telescopes will complement future space-based missions planning to image planets in reflected visible light. Direct imaging at $3-10\mu m$ of terrestrial planets orbiting Sun-like stars could provide knowledge on thermal emissions that will inform future visible light observations (Quanz et al. 2014).

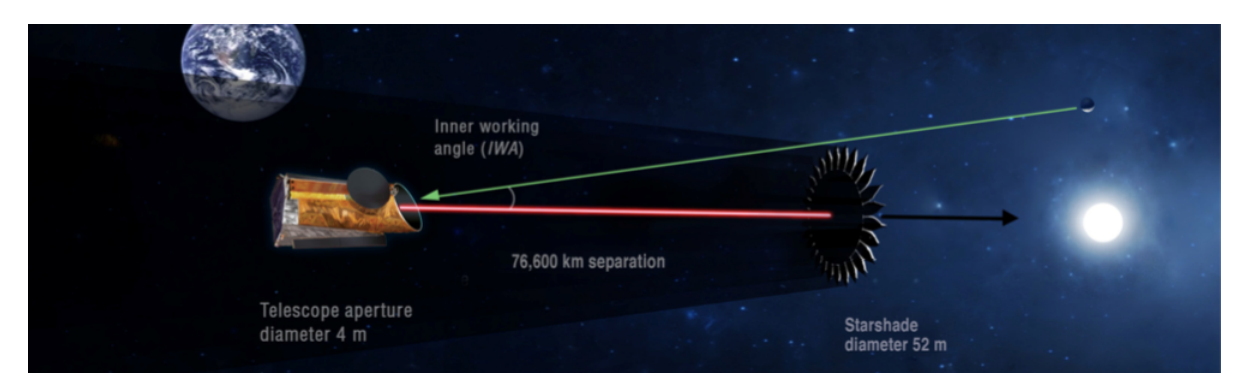


Figure 1.4: The HabEx telescope flying with the starshade. Planets can be detected near and beyond the edge of the starshade which defines the IWA (Gaudi et al. 2020).

Space based telescopes designed to directly image exoplanets have yet to be launched. In May 2027, the Nancy Grace Roman Space Telescope (formerly known as WFIRST) will lift off, and will be equipped with a Coronagraph Instrument (CGI). The CGI will serve as a technology demonstration for future space-based missions planning to directly image planets in visible light from the host star reflected off the planet. Roman will be the first telescope capable of directly imaging known mature Jupiter analogs at these wavelengths (Kasdin et al. 2020a). The CGI is expected to be 100 to 1000 times better than any current ground-based facility, having a threshold requirement of 10⁻⁷ contrast (Kasdin et al. 2020a). This will help pave the way for future space-based missions like the Habitable Exoplanet Observatory (HabEx) and the Large Ultraviolet Optical Infrared Surveyor (LUVOIR). In particular, flying the CGI will demonstrate how a coronagraph interacts with the entire telescope and its control systems, which will drastically reduce the risk of including sensitive optical equipment on future missions (Kasdin et al. 2020a).

Missions like HabEx and LUVOIR are planned to launch in the 2040s (and will most likely be combined into one mission). Following the planned science goals of Roman, these missions will be able to image faint Earth-twins orbiting Sun-like stars in reflected visible light, and will arguably become the best way of finding such planets at all (Gaudi et al. 2020; The LUVOIR Team 2019a). Because of the

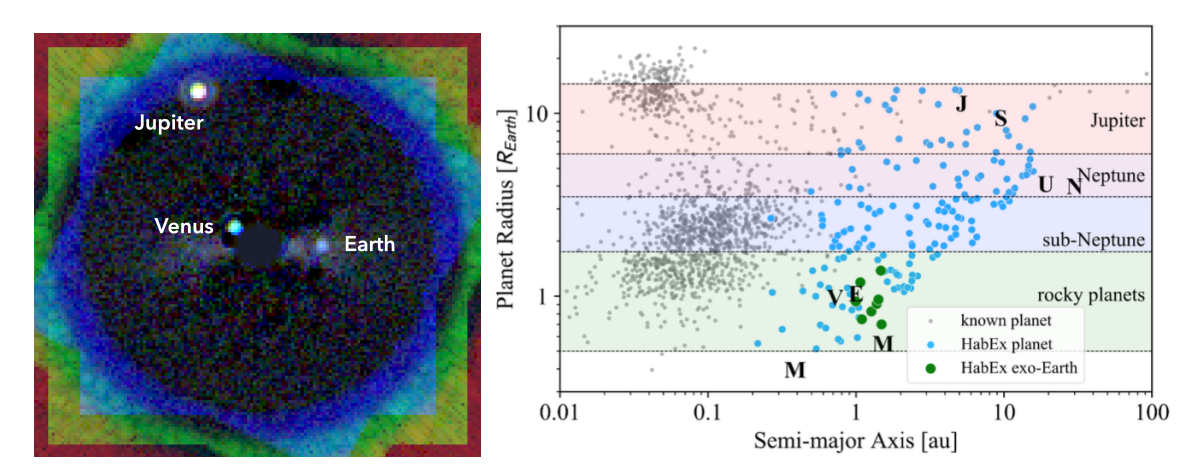


Figure 1.5: Left: A simulation of the Solar system as seen by LUVOIR in visible light at a distance of 10 pc (The LUVOIR Team 2019a). Right: Expected distribution of exoplanets discovered by HabEx plotted by Earth-radius (AU) and semi-major axis (AU) on log-scales. Expected exoplanet discoveries are shown in blue, or green if these are exo-Earths. Grey dots are known exoplanets (Gaudi et al. 2020).

inherent biases of other exoplanet detection methods (mainly radial velocity and transits), direct imaging is the strongest contender for characterizing rocky planets on longer orbital periods. HabEx and LUVOIR have been identified in the 2021 Decadal Survey as important missions "positioned to make a serious attempt at searching for biosignatures on exoearth candidates" (National Academies of Sciences 2021). The right image of Figure 1.5 indicates the expected yield of HabEx, with exo-Earths shown in green. Both missions intend to image stars at a maximum distance of 10 pc (The LUVOIR Team 2019a; Gaudi et al. 2020). LUVOIR would include the Extreme Coronagraph for Living Planetary Systems (ECLIPS) which would have imaging cameras spanning 200-2000 nm (The LUVOIR Team 2019a). A simulation of our own Solar system as seen by LUVOIR at 10 pc in visible light is shown on the left of Figure 1.5. Alternatively, there would be a HabEx Coronagraph (HGC) designed to achieve similar performance goals as ECLIPS, with an expected bandpass of 450-1800 nm (Gaudi et al. 2020). In particular, the design plan of HabEx has includes the use of a starshade to block out starlight, that would fly independently from the telescope and position itself in between the telescope and the star-planet system. Figure 1.4 shows what the starshade would look like flying in formation with the telescope. While a coronagraph's resolution depends on the incoming wavelength and telescope diameter, resolution with a starshade would depend on its diameter and its distance from the telescope (Gaudi et al. 2020). Including both instruments allows each one to complement the weaknesses of the other. While coronagraphs are ideal for blind exoEarth searches and orbit

determination, the starshade is ideal for wide-field mapping of planetary systems and spectral characterization (Gaudi et al. 2020).

Both LUVOIR and HabEx mission designs have planned out how they will achieve the $\sim 10^{-10}$ contrast required to image nearby Earth-twins around Sun-like stars, following the advances achieved by preceding missions. A fiducial 2 year survey optimized for Earth-like exoplanets with a mission like LUVOIR is expected to find almost ~ 20 – 60 of these targets, based on population studies by Stark et al. (2014a), and as shown in Figure 1.6.

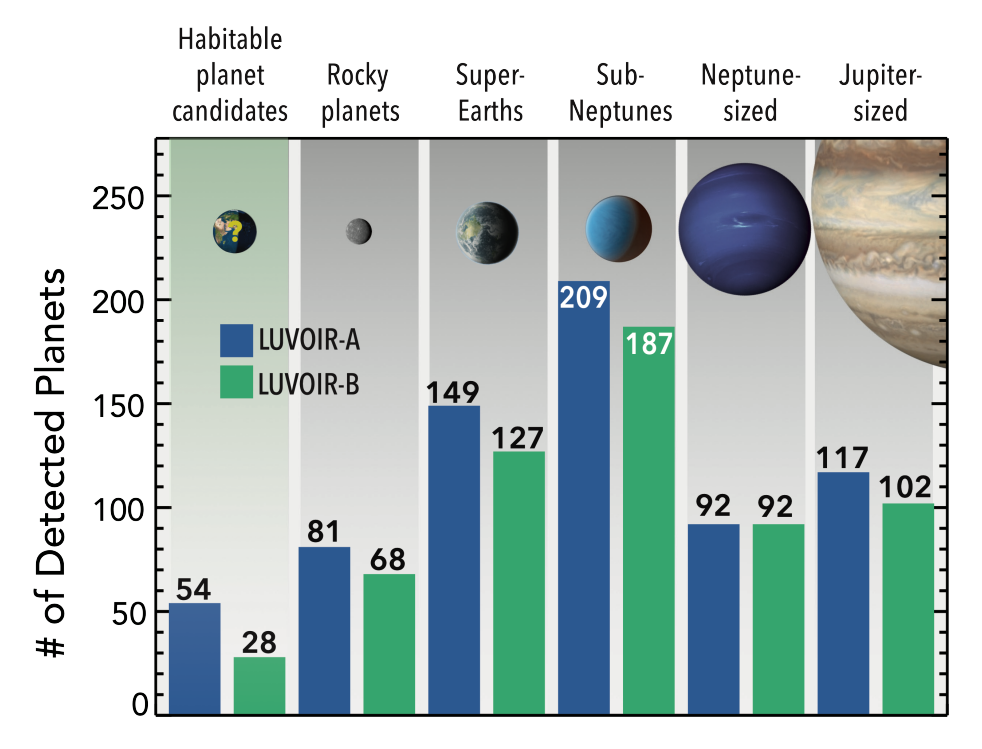


Figure 1.6: Detection yields for different exoplanet types from a 2 year habitable planet survey with two different LUVOIR design options. LUVOIR-A (blue bars) would have a 15 m mirror, and LUVOIR-B (green bars) would have an 8 m mirror. Planet types are organized by panel. From left to right these are: exoEarth candidates, rocky planets, super-Earths, sub-Neptunes, Neptunes, and Jupiters. (The LUVOIR Team 2019a).

1.4 Orbit Retrieval

Directly detecting an exoplanet is a great opportunity to determine its orbit. Each direct image provides the two-dimensional position of the planet relative to the star in the sky plane, which we call a planet's astrometry. Multiple images can uniquely

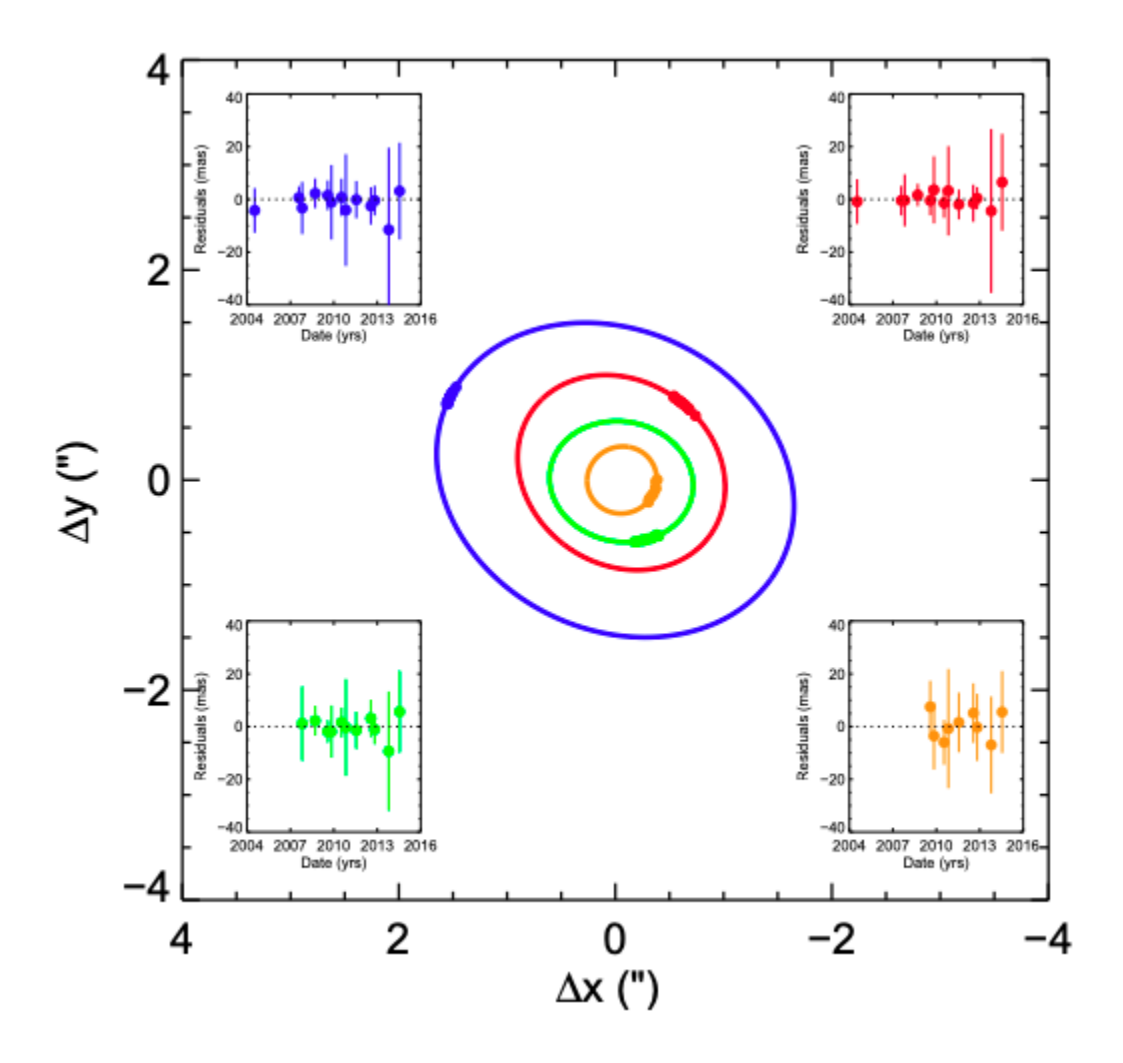


Figure 1.7: Sample orbits determined by Konopacky et al. (2016a) consistent with observational data of the HR 8799 system. Each orbit is within 1σ of the best fit solution, with residuals indicated in the four side panels.

determine a planet's orbital path and help constrain it's mass. The separation between a planet and host star and their mass ratio can hint at possible formation pathways, since theoretical models rely on these (Lagrange 2014). Additionally, a planet's orbit can indicate whether it is in the habitable zone (HZ) of its host star and provide clues regarding its climate.

Numerical methods are typically used to retrieve a planet's orbit from its astrometry. Keplerian orbits are governed by 6 parameters outlined in Table 2.1 in Section 2.2.1. Markov-chain Monte Carlo (MCMC) methods estimate the posterior distributions of the orbital elements being sampled. More details on these methods are outlined in subsequent sections of this thesis.

Orbit retrieval has been performed on previously imaged exoplanet systems. In particular, there has been a significant analysis of the HR 8799 system. The four young super-Jupiters in the HR 8799 system are located very far from the host star (~ 15 to 70 AU) and thus have very long orbital periods. Astrometric data from this system have been collected in the years following the initial discovery by Marois et al. (2008, 2010), but only a very small fraction of the planet's orbital periods have been imaged (~ 3 to 12%). Thus, determining an allowed family of orbits can be computationally challenging. A nice example of orbit retrieval on these exoplanets comes from Konopacky et al. (2016a), where the astrometry from 13 observations was used to determine the orbits shown in Figure 1.7. Later, an analysis by Wang et al. (2018a) agreed with these results. Earth-twins would of course have orbital periods of approximately one year, making it a lot easier to observe such planets over a larger fraction of their orbit, and fewer images would be required to properly constrain their path. Direct images of terrestrial planets require long exposure times, meaning each one is very costly and time consuming. As such, future missions are interested in reducing the number of images required to determine whether an Earth-twin is in the HZ. One way this can be done is by considering the brightness of the planet in reflected visible light. Each direct image of course provides the 2D planetary astrometry (x,y) with the star at the origin (0,0). At visible wavelengths, the photometry is dominated by reflected light, which varies throughout its orbit — phase variations — adding a third time-dependent quantity to each direct image. This thesis explores how the addition of photometric data improves both the accuracy and precision of retrieved orbits compared to analyses done solely with astrometry. The benefits of photometry for the orbit retrieval of a particular Earth-twin is shown in Figure 1.8. In this case, a model which uses astrometric and photometric information provides a more constrained retrieval than a model which uses astrometry alone. We hence show how photometry reduces the number of images required to properly constrain an orbit, and significantly improves the accuracy of orbit retrieval more generally.

1.5 Numerical Methods

1.5.1 Bayesian Statistics

The numerical tools used to determine orbits from astrometric and photometric data rely on Bayesian statistics. To do this, parameters are given a prior probability distribution which expresses one's beliefs about the quantity before being given any evidence. For example, an angular Keplerian orbital parameter like the argument of

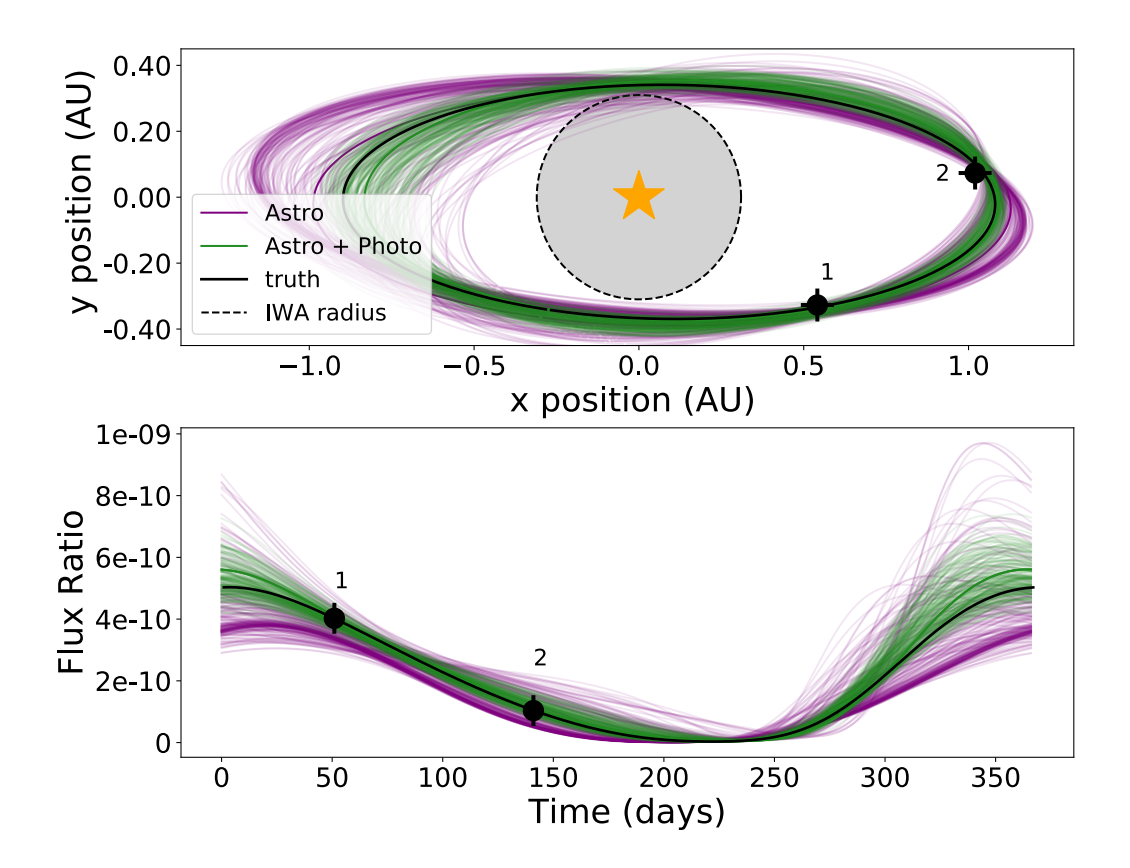


Figure 1.8: Top panel: Orbit retrievals for an exoplanet detected twice. Bottom panel: Planet/star flux ratio retrievals for the same exoplanet. Solid black lines indicate the true orbit and phase curve generated by the model. Black points indicate each direct image (90 days apart) with their corresponding error (0.01 AU for astrometry and 10⁻¹² for photometry), which are inflated to be visible. The gray circle around the host star represents the area covered by the IWA of the telescope. The coloured lines are drawn from kombine (see Section 1.5.2). Purple lines demonstrate orbit and phase retrievals for a model which used only astrometric information. Green lines demonstrate orbit and phase retrievals for a model which used astrometric and photometric information.

periapsis would be given a uniform prior distribution between 0 and 2π because it could be any quantity in this range. These prior distributions are combined with observational data in the form of a likelihood function to update our knowledge of a given parameter. A likelihood function describes how likely it is that given parameters describe the observed data. This combination of a prior and a likelihood

is called a posterior distribution and summarizes the updated probability distribution of a parameter given the data. In short, given a prior distribution $p(\theta)$ and that the observed data x have a likelihood $p(x|\theta)$, then the posterior probability is:

$$p(\theta|x) = \frac{p(x|\theta)}{p(x)}p(\theta), \tag{1.1}$$

where p(x) is a normalizing constant given by $p(x) = \int p(x|\theta)p(\theta)d\theta$ (Spiegelhalter & Rice 2009).

1.5.2 Markov chain Monte Carlo methods

Markov chain Monte Carlo (MCMC) is used to determine posterior distributions for parameters. Monte Carlo simulations estimate parameters by repeatedly generating random nearby locations in parameter space and probabilistically deciding whether to move to that new location. This is an efficient computational tool used for sampling probability distributions, particularly when an analytic method is unavailable. Monte Carlo methods are typically used for three reasons: to estimate the distribution of a target function, to approximate a quantity like the mean or variance of a distribution, or to optimize a function by locating a sample that maximizes or minimizes it. In a Bayesian context, any posterior distribution $p(\theta|x)$ can be approximated by taking many random samples of a parameter from the posterior (Spiegelhalter & Rice 2009).

MCMC methods are often used in a Bayesian context. Astrophysical data analysis often requires computing the posterior probability density function of parameters in a model, and MCMC methods are well suited to sample these high-dimensional parameter spaces. Random walks are set up to explore parameter space and sample the posterior distributions of the desired parameters. The most commonly used MCMC algorithm is the Metropolis-Hastings method. Walkers will perform the following iteration: 1) given a position X(t), sample the next proposal position Y from a transition distribution, often a multivariate Gaussian centered on X(t), 2) accept the proposal position with some probability related to the ratio of posterior probabilities at the proposed and current locations in parameter space. If the proposal position is rejected, the new position is set to the previous one (Foreman-Mackey et al. 2013b). The algorithm ends when the random walks converge on a common solution. Meaning, all the walkers have moved to the same area of parameter space with the highest likelihood.

Put more simply, when trying to determine probability density functions (PDFs)

for parameters in a model, MCMC codes can randomly select a point in the allowed parameter space and evaluate the posterior of the corresponding model. Then, the posterior of a model at a nearby point is also evaluated. If this new position is a better fit to the data (a higher posterior) then the chain will move there, and repeat the process until the best solution is found (when there are no higher posteriors).

Sometimes the chain will determine that a nearby point has a lower posterior, but will move there anyway. To efficiently sample the entire PDF. The 'decision' of whether or not to move to a worse position is made by generating a random number between 0 and 1, and comparing it to the ratio of the posteriors at the new versus old position in parameter space. If the random number is less than this ratio, the chain will move to the new position.

Astronomers often use the open source Python package emcee developed by Foreman-Mackey et al. (2013b), which acts as a user-friendly MCMC ensemble sampler to perform the functions described above. Additionally, the research in this work uses a similar package called kombine developed by Farr & Farr (2015), which is particularly efficient for poorly constrained, or degenerate, problems. When a planet is only detected twice, there are fewer data points than parameters to solve for. There could be many solutions (orbits) such that the program cannot determine which is more likely — since there is less information available to constrain the solution. Here, kombine is more useful than emcee because it was specifically built to efficiently evaluate multimodal distributions, with many maxima and minima (Farr & Farr 2015). kombine uses estimates of the walker's instantaneous posterior distribution as a proposal position, making it easier for the program to localise on an area of high probability without getting 'lost'. (Farr & Farr 2015).

Chapter 2

Combining Photometry and Astrometry to Improve Orbit Retrieval of Directly Imaged Exoplanets

This thesis chapter has been accepted for publication to the Monthly Notices of the Royal Astronomical Society and is in press, and appeared in pre-print as:

Margaret Bruna, Nicolas B. Cowan, Julia Sheffler, Hal M. Haggard, Audrey Bourdon, Mathilde Malin, arXiv:2208.08447v1 [astro-ph.EP]

2.1 Introduction

Direct imaging is the most promising approach for characterizing planets orbiting in the habitable zone of Sun-like stars, and is arguably the best way to discover such planets in the first place. Future direct imaging missions like the Nancy Grace Roman Space Telescope, HabEx, and LUVOIR will be capable of detecting visible light reflected by exoplanets (The LUVOIR Team 2019b; Gaudi et al. 2020; Kasdin et al. 2020b). The 2021 Decadal survey has identified HabEx and LUVOIR as important missions "positioned to make a serious attempt at searching for biosignatures on exoearth candidates" (National Academies of Sciences 2021). One of the first properties we seek to determine when characterizing an exoplanet is its orbit, most importantly its semi-major axis, which in conjunction with its star's

luminosity is the principal determinant of a planet's climate. We would like to determine the orbit with as few imaging epochs as possible (e.g., Stark et al. 2014b).

2.1.1 Orbit retrieval via planetary astrometry

Previous efforts to retrieve orbits of directly imaged planets focused on the time-varying position of the planet in the sky plane, i.e., planetary astrometry. This is because current direct imaging efforts are primarily sensitive to thermal emission from young Jovian planets (Marois et al. 2008a, 2010; Macintosh et al. 2015; Lagrange et al. 2019). Since the planets are self-luminous, they do not exhibit phase variations and only the changing projected position of a planet betrays its orbit. Indeed, many researchers have used astrometry to constrain the orbits of the four directly imaged planets around HR 8799, despite their long orbits (Sudol & Haghighipour 2012; Pueyo et al. 2015; Currie 2016; Konopacky et al. 2016b; Blunt et al. 2017; Wang et al. 2018b).

Studies of direct imaging in reflected light have also focused on planetary astrometry for orbit retrieval. Compared to current thermal imaging, reflected light direct imaging favours planets on shorter orbits. This is better for constraining retrievals, since it is easier to image a larger fraction of the entire orbit. Guimond & Cowan (2019) examined the optimal number, cadence, and precision of direct imaging observations required to establish the orbit of a planet. They showed that a few epochs provide useful orbital constraints, even when some epochs are non-detections. Moreover, they demonstrated that 3 equally spaced epochs at least 90 days apart are sufficient to uniquely constrain a planet's orbit. Meaning, the semi-major axis is constrained to within 10% of the true value and the posterior in singularly peaked rather than multimodal. For three or more epochs, the precision on the semi-major axis is approximately the astrometric precision multiplied by the distance to the system, e.g., three epochs of 5 mas planetary astrometry of a system 10 pc away constrains the semi-major axis to approximately 5 mas \times 10 pc = 0.05 AU. These conclusions have since been independently confirmed by Horning et al. (2019) and Romero-Wolf et al. (2021).

2.1.2 Phase variations for orbit retrieval

Future direct imaging missions operating in the optical and near-infrared will be sensitive to scattered light from exoplanets. As a distant planet orbits its star, its brightness varies as we see more of less of its illuminated hemisphere (Galilei 1610),

so-called phase variations. We hypothesise that a planet's time-varying photometry could help constrain its orbit with fewer epochs of direct imaging, and significantly reduce the uncertainty on retrieved orbital parameters given the same number of epochs.

In Section 2 we describe our numerical experiment. Section 3 presents the results of orbital retrievals for planets detected at two, three, and four epochs and for a variety of astrometric and photometric uncertainties. We compare models that retrieve planets exibiting Lambertian phase curves and ones which reflect light irregularly and have a Henyey-Greenstein phase function. In Section 4 we discuss the impact of these results on the design of future missions.

2.2 Methods

2.2.1 Keplerian Orbits and Henyey-Greenstein Phase Curves

The projected sky position of a planet moving on a Keplerian orbit is given by (Murray & Correia 2010):

$$x = r \Big(\cos\Omega \cos(\omega + \nu) - \sin\Omega \sin(\omega + \nu) \cos i \Big)$$
 (2.1)

and

$$y = r \Big(\sin\Omega \cos(\omega + \nu) + \cos\Omega \sin(\omega + \nu) \cos i \Big)$$
 (2.2)

where the planet-star separation is

$$r = \frac{a(1 - e^2)}{1 + e\cos E}. (2.3)$$

In the above, Ω is the longitude of ascending node, ω is the argument of periapsis, ν is the time-dependent true anomaly, i is the inclination, a is the semi-major axis, e is the eccentricity, and E is the eccentric anomaly.

Synthetic planets are generated using the parameter distributions outlined in Table 2.1. The time dependence of the true anomaly, ν , is computed using Newton's method. To produce and retrieve orbits, we reparameterize our model using the mean anomaly, M, because it has a uniform prior over $(0, 2\pi)$:

$$M = E - e\sin E \tag{2.4}$$

CHAPTER 2. ORBIT RETRIEVAL USING PLANETARY ASTROMETRY PHOTOMETRY

Parameter	Symbol	Input Distribution	Prior Distribution
Semi-major axis	$\ln a$	a = 1 AU	$\mathcal{U}[\ln 0.01\mathrm{AU}, \ln 50\mathrm{AU}]$
Eccentricity	e	$B(\alpha = 0.867, \beta = 0.303)$	$B(\alpha = 0.867, \beta = 0.303)$
Inclination	$\cos i$	$\mathcal{U}[\cos 0, \cos \pi/2]$	$\mathcal{U}[\cos 0, \cos \pi]$
Argument of periapsis	ω	$\mathcal{U}[0,2\pi)$	$\mathcal{U}[0,2\pi)$
Longitude of ascending node	Ω	$\mathcal{U}[0,2\pi)$	$\mathcal{U}[0,2\pi)$
Mean anomaly of first epoch	M_o	$\mathcal{U}[0,2\pi)$	$\mathcal{U}[0,2\pi)$
Albedo figure of merit	$\ln AR_p^2$	$AR_p^2 = 0.3R_{\oplus}^2$	$\mathcal{U}[\ln(0.01R_{\oplus}^2), \ln R_{\mathrm{Jup}}^2]$
Heyney-Greenstein parameter	g	$g = 0 \text{ or } \mathcal{N}(0, 0.7)$	$g = 0 \text{ or } \mathcal{N}(0, 0.7)$

Table 2.1: Six Keplerian parameters (top) and two phase curve parameters (bottom). The input distributions are used when generating synthetic planets, while the prior distributions are used when retrieving orbits. These distributions are the same except for the semi-major axis, a, and the reflection figure of merit, AR_p^2 . The input semi-major axis, albedo and radius correspond to those of Earth so that all of our synthetic planets are Earth-like. Their priors, on the other hand, are broad and log-uniform because planets tend to be small and on close orbits. For orbital eccentricity we use a beta distribution with $\alpha = 0.867$ and $\beta = 0.303$ (Nielsen et al. 2008; Kipping 2013).

where the eccentric anomaly is related to the true anomaly via

$$\tan E = \frac{\sqrt{1 - e^2} \sin \nu}{e + \cos \nu}.\tag{2.5}$$

We adopt the mean anomaly at the first epoch, M_0 , as our initial condition:

$$M = M_o - \frac{2\pi}{T}(t - t_o), \tag{2.6}$$

where t_o is the first epoch, t is time, and T is the orbital period. Since mean anomaly advances at a constant rate throughout a planet's orbit, the prior on M_0 is also uniform over $(0, 2\pi)$.

The reflected flux ratio of the planet to its host star is (Charbonneau et al. 1999):

$$\epsilon(\Phi) \equiv \frac{f_p(\Phi)}{f_{\star}} = A_g P_{\rm HG}(\Phi, g) \frac{R_p^2}{r^2},\tag{2.7}$$

where $A_{\rm g}$ is the geometric albedo, $P_{\rm HG}(\Phi,g)$ is the phase function, and R_p is the planetary radius.

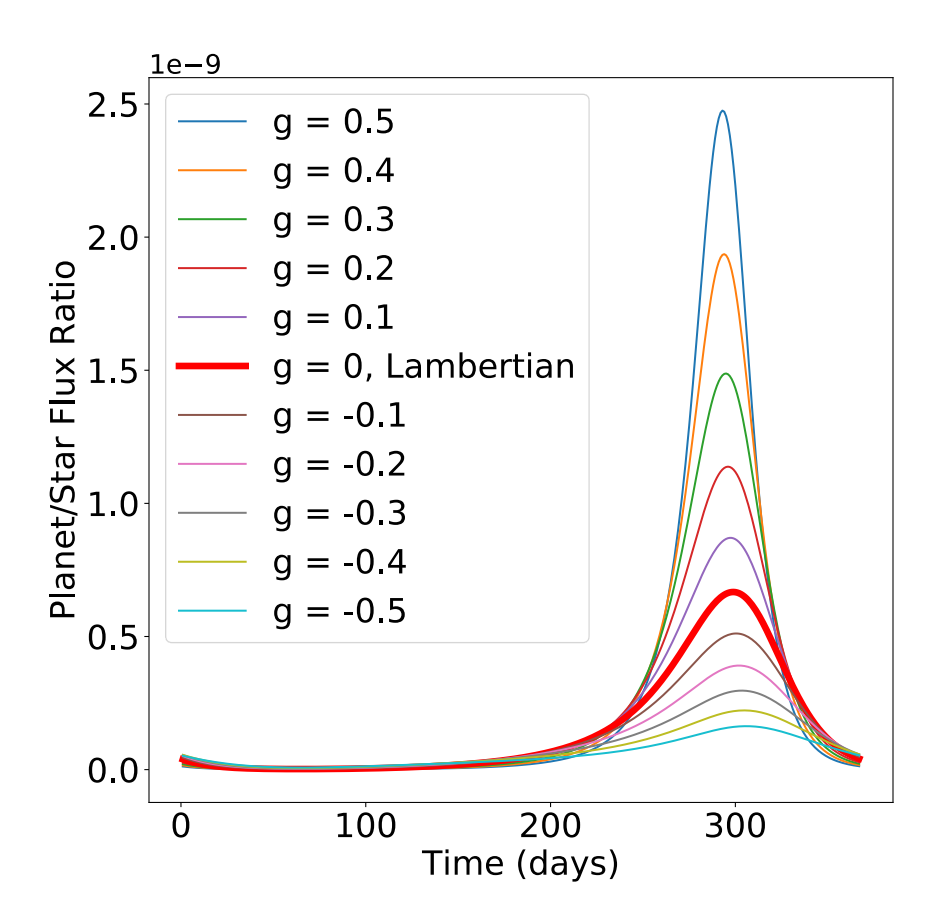


Figure 2.1: Brightness model produced by the Henyey-Greenstein phase function for a scattering parameter g ranging from -0.5 to 0.5. The curves are generated with a=1.00 AU, e=0.31, $\cos i=0.41$, $\omega=2.25$ rad, $\Omega=3.38$ rad, and $M_o=3.87$ rad, and $AR_p^2=3.63\times 10^{-10}$ AU² (where A=0.3 and $R_p=R_{\oplus}$).

We adopt the phase curve parameterization of Henyey & Greenstein (1941):

$$P_{\rm HG}(\Phi, g) = \frac{1 - g^2}{(1 + g^2 - 2g\cos\Phi)^{\frac{3}{2}}} \left(\frac{\sin\Phi + (\pi - \Phi)\cos\Phi}{\pi}\right),\tag{2.8}$$

where the star–planet–observer phase angle Φ is given by

$$\cos \Phi = \sin(\omega + \nu) \sin i. \tag{2.9}$$

For g = 0 the scattering is diffuse (i.e isotropic) (Lambert 1760), $P_{\rm HG}$ reduces to the Lambertian phase curve (Russell 1906) and the brightness is the same regardless of the observer's point of view. Figure 2.1 shows example HG phase variations as function of time and for different scattering parameters g. When g > 0 the function describes forward scattering, and g < 0 corresponds to backward scattering. More precisely, g is the average value of the product of the phase function and the cosine of the angle between the incident and scattered ray.

2.2.2 Synthetic planets and observations

We generate 100 synthetic Earth-like planets and for each one we produce synthetic astrometric and photometric data for 2, 3, and 4 epochs. We choose this sample size because our results are unchanged if the number of synthetic planets is doubled.

We randomly generate the six Keplerian and two phase curve parameters according to the distributions outlined in Table 2.1 to produce an orbit and a phase curve. We assume single planet systems for the entirety of this experiment and we enforce that each direct-imaging epoch yields a detection of the planet. The detections-only simplification minimally impacts our results, as we discuss in Section §2.4.3.

All of our synthetic planets have a semi-major axis of a=1 AU, an albedo of A=0.3, and the radius of the Earth, $R_p=R_{\oplus}$. The orbital eccentricity, e, is drawn from a beta distribution (Nielsen et al. 2008; Kipping 2013), the orbital inclinations, i are isotropic (uniform in $\cos i$), while the argument of periastron, ω , longitude of ascending node, Ω , and mean anomaly at the first epoch, M_0 , are drawn from uniform distributions.

Following Guimond & Cowan (2019), we set the distance to the star-planet system to 10 pc and adopt an inner working angle (IWA) of 30 mas, corresponding to a minimum projected separation of 0.3 AU. We produce images at each epoch given a fixed 90-day cadence (Guimond & Cowan 2019). We add Gaussian astrometric noise of $\sigma_{\rm astro}$ to the projected x and y positions of the planet and $\sigma_{\rm photo}$ to the

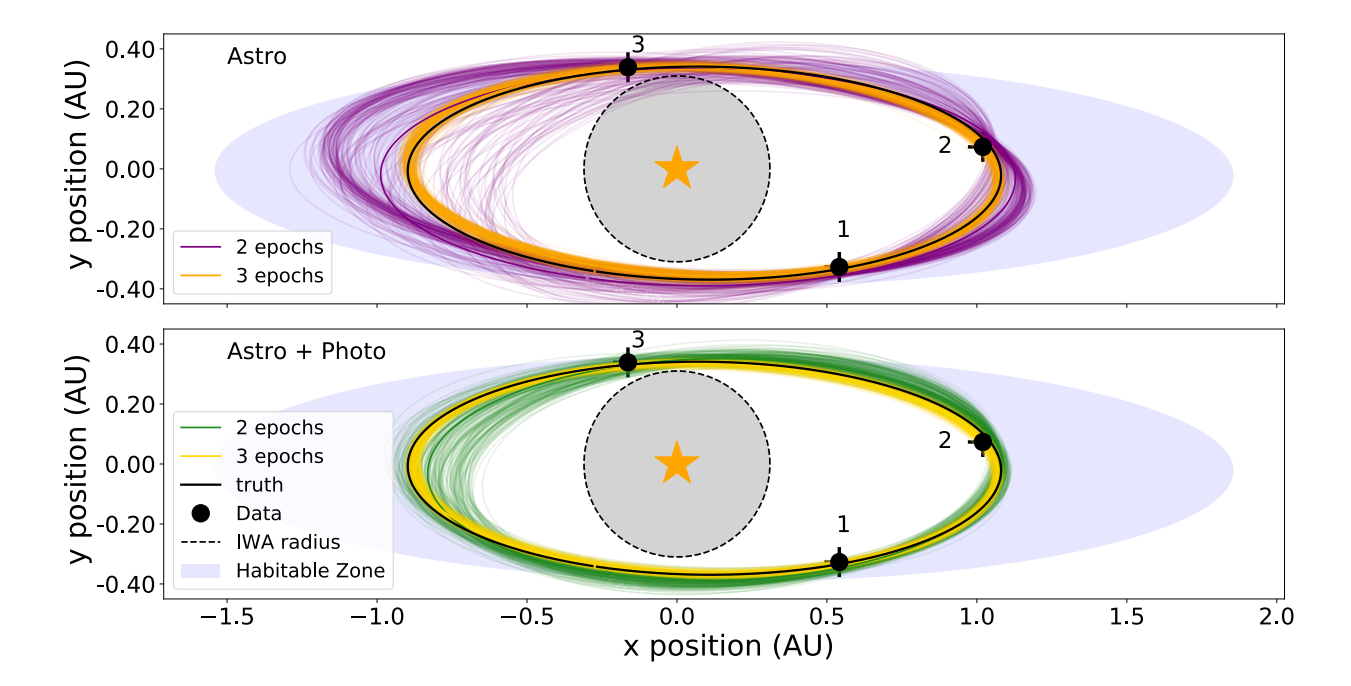


Figure 2.2: Orbit retrievals for an exoplanet after 2 and 3 detections. The top panel demonstrates orbital retrievals using only astrometry, and the panel below demonstrates retrievals using astrometry and photometry. The colored lines are draws from kombine in the 2 epoch case, and from emcee in the 3 epoch case. The black line is the true orbit of the synthetic planet, and the black data are the astrometry at the three epochs. The astrometric uncertainties of 0.01 AU have been inflated $5\times$ to be visible. The gray circle around the host star indicates the area obscured by a notional coronagraph or starshade. The lavender shaded region indicates the habitable zone predicted by Kopparapu et al. (2013).

planet/star flux ratio; we also adopt these values for the astrometric and photometric measurement uncertainties. We show example multi-epoch observations in Figure 2.2.

2.2.3 Retrieving orbital and phase parameters

Retrieving orbital and phase parameters entails performing fits to astrometric and photometric data. For astrometric fits to N epochs we define the usual badness-of-fit,

$$\chi_{\text{astro}}^2 = \sum_{i=1}^N \frac{(x_i - x_{m,i})^2 + (y_i - y_{m,i})^2}{\sigma_{\text{astro}}^2},$$
(2.10)

where x_i and y_i are the measured location of the planet at the *i*th epoch while $x_{m,i}$ and $y_{m,i}$ are the model prediction for that epoch.

For retrievals using both astrometry and photometry we define the total badness-of-fit as $\chi^2 = \chi^2_{\rm astro} + \chi^2_{\rm photo}$, where the photometric badness-of-fit is

$$\chi_{\text{photo}}^2 = \sum_{i=1}^N \frac{(\epsilon_i - \epsilon_{m,i})^2}{\sigma_{\text{photo}}^2}.$$
 (2.11)

Here ϵ_i and $\epsilon_{m,i}$ are the measured and predicted planet-to-star flux ratio.

Posterior Sampling

We begin each retrieval by performing a χ^2 minimization using scipy.optimize to obtain a first guess of the best fit parameters. We then use ensemble samplers emcee (Foreman-Mackey et al. 2013a) and kombine (Farr & Farr 2015) to retrieve the posterior distributions on orbital and phase parameters. These Bayesian codes require a likelihood function, which we define as $\ln L = -\chi^2$, and a prior probability distribution for the fitted parameters.

With the exception of semi-major axis a and the reflected light figure of merit AR_p^2 , we adopt as priors the same distributions used to generate the synthetic planets. For semi-major axis and AR_p^2 we adopt log-uniform priors to encode that there are more planets orbiting closer to stars and there are more small planets. Our priors are listed in Table 2.1.

For under-constrained retrievals (2 epochs) we use kombine, which uses a clustered kernel-density-estimate proposal that allows for more efficient sampling when plausible solutions are spread out in parameter space, as one would expect

for a formally degenerate problem. We use 500 walkers that take 800 to 8000 steps, with burn-in ranging from 300 to 3000 steps; kombine checks for convergence automatically, so the number of steps for a particular run varies from one fit to another.

For marginally- or over-determined problems (3 or more epochs) we use emcee to retrieve posterior distributions on the Keplerian and phase parameters. We use 50-100 walkers that run for 5000-15000 steps, depending on the model in question. For both kombine and emcee we check for convergence by examining the corner plots and walker plots produced. As a spot check, we repeated some of the 3-epoch retrievals using kombine to ensure that the resulting posteriors were indistinguishable from those obtained with emcee.

Figure 2.2 shows an orbit retrieval for 2 and 3 epochs with and without photometry. The precision of our retrieval depends on the use of photometry, which adds one datum per epoch but also one or two fitted parameters, depending on the choice of phase curve parameterization.

The retrieved parameters are compared to the true values for that synthetic planet to determine the bias and accuracy of the retrievals. The discrepancy between the retrieved parameter and its true value is denoted by Δ . For a given parameter, the mean discrepancy for a large number of synthetic planets is an estimate of the retrieval bias, $\langle \Delta \rangle$, while the standard deviation of these same discrepancies is an estimate of the retrieval accuracy σ_{Δ} . We tabulate bias and accuracy for all fitted parameters, but we focus on the semi-major axis because it is the primary discriminant for identifying potentially habitable planets, a stated goal of next generation direct imaging missions.

Number of epochs

We consider scenarios with detections of the planet at 2, 3, or 4 epochs. Purely astrometric retrievals of 2 epochs use 4 data to retrieve 6 parameters. Meanwhile, photometric + astrometric retrievals of 2 epochs fit 6 data with 7–8 parameters, depending on the assumed scattering phase function. Thus orbit retrieval based on 2 epochs of direct imaging is always under-constrained. With 3 detections of the planet, astrometric + photometric retrieval fits 9 data to retrieve 7–8 parameters, while retrievals based solely on astrometric information fit 6 data with 6 parameters. With detections at 4 epochs, the orbit is over-determined regardless of whether photometry is considered, so retrieval is an optimization problem.

Astrometric and photometric uncertainty

We adopt fiducial uncertainties of $\sigma_{\rm astro}=0.01$ AU for astronometry and $\sigma_{\rm photo}=10^{-12}$ for photometry (relative to the planet/star flux ratio). Our fiducial astrometric uncertainty is smaller than that used by Guimond & Cowan (2019) or Romero-Wolf et al. (2021)— it is meant to mimic the limit of infinitely precise astrometry in order to focus on the intrinsic degeneracies of the retrieval problem in the 2 epoch case. In order to test the impact of astrometric uncertainty, especially in the over-determined 3 and 4 epoch cases, we repeat our experiment with more realistic errors of $\sigma_{\rm astro}=0.035$ AU (Guimond & Cowan 2019). For completeness, we also experiment with greater photometric uncertainties of $\sigma_{\rm photo}=3.5\times 10^{-12}$. To put these values in perspective, the intrinsic degeneracy in the single epoch case leads to uncertainties of $\sigma_a=0.29$ –1.04 AU (see §3.1), while the amplitude of orbital phase variations for an Earth-twin are on the order of 10^{-10} .

Scattering function for phases

We consider two scenarios regarding prior knowledge of the planet's scattering phase function. In the optimistic case we have good prior knowledge: we assume the same HG parameter in the retrieval as we use to produce the synthetic phase curves (g = 0 in both cases, i.e., Lambertian phase curves all around). In the realistic scenario, synthetic planets have randomly generated g drawn from a Gaussian distribution inspired by Solar system worlds. We fit for g as part of our retrieval, using the same Gaussian distribution as our prior (see Table 2.1 for details).

2.3 Results

2.3.1 Single epoch posterior on semi-major axis

Before presenting the results of our orbit retrievals for multi-epoch direct-imaging campaigns, it is useful to consider the orbital information present in a single epoch. A single epoch of direct imaging (Marois et al. 2008b) or planetary microlensing (Gould & Loeb 1992) provides a measurement of the planet's projected separation from its host star. The instantaneous projected separation places constraints on the planet's semi-major axis: to first order, the two are equal. In detail, the posterior distribution for semi-major axis depends on the choice of priors for semi-major axis and orbital eccentricity.

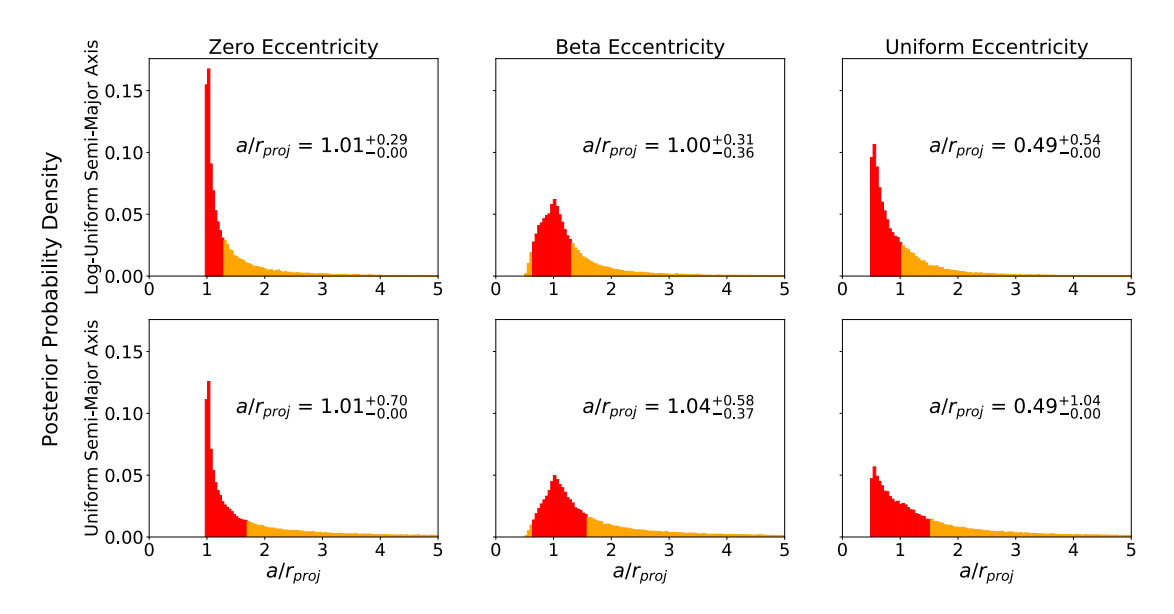


Figure 2.3: A single measurement of r_{proj} from direct imaging or planetary microlensing constrains the planet's semi-major-axis. Each panel shows the posterior probability distribution of $a/r_{\rm proj}$ for different prior distributions on semi-major axis and eccentricity. The prior on semi-major axis is either log-uniform (top row) or uniform (bottom row). The eccentricity is either set to 0 (left column), given a beta distribution (middle column), or uniform distribution (right column). Concretely, if a single epoch of infinitely precise astrometry shows the planet to have a projected separation of $r_{\text{proj}} = 1 \text{ AU}$, then the x-axis is simply the semi-major axis of the planet in AU; for imprecise astrometry, these distributions would have to be convolved with a Gaussian representing the measurement uncertainty. The peaks in the data therefore correspond to the most probable semi-major axis and the red bins show the 1σ (68% confidence) interval. The top-left panel has the most optimistic priors: the posterior peaks very close to the true value and has an asymmetric 1σ interval spanning 0.29 AU. The bottom-right panel has the most pessimistic priors: the posterior is severely biased and the 1σ interval spans 1.04 AU. The top-center panel is the most realistic case: the posterior is essentially unbiased and the 1σ interval spans 0.67 AU.

$CHAPTER~2.~~ORBIT~RETRIEVAL~USING~PLANETARY~ASTROMETRY\\PHOTOMETRY$

We generate 5 million planets with the prior distributions shown in Table 2.1, and retrieve those with projected separations of $r_{\text{proj}} \equiv \sqrt{x^2 + y^2} \in [0.99, 1.01]$ AU. Note that for single-epoch observations, the projected separation is the only useful datum: the x and y positions are not useful on their own, while we conservatively neglect the marginal information content in a single epoch of planetary photometry (Guimond & Cowan 2018; Bixel & Apai 2020). We show in Figure 2.3 the posterior probability densities for the scaled semi-major axis, a/r_{proj} . The peaks in the data therefore correspond to the most probable semi-major axis and the red bins show the 1σ (68% confidence) interval. Concretely, if a single epoch of direct imaging shows a planet at a projected separation of $r_{\text{proj}} = 1$ AU, then these are simply the posterior distributions on the semi-major axis. We adopt a uniform or log-uniform prior on semi-major axis in astronomical units. This choice has a negligible impact on the posterior peak, but changes the width of the posterior as expected: log-uniform favours shorter a leading to narrower distributions.

The prior on eccentricity is either a delta function fixed to 0 (for planets with circular orbits), a beta distribution (the same as outlined in Table 2.1), or uniform. These significantly impact the overall shape of the distribution and the peak of the posterior. With a uniform eccentricity the peak of the scaled semi-major axis is at 0.5 because a planet with an eccentricity of 1 will spend the majority of its orbit near apastron, which is approximately located at a distance of $r_{\rm proj} \lesssim 2a$ away from the star. The single-epoch projected separation provides an approximately unbiased estimate of the semi-major axis if the eccentricity is zero or described by a beta distribution, but overestimates the semi-major axis by a factor of two for uniformly-distributed eccentricities. In many other astrophysical contexts eccentricity is expected to have a thermal distribution, where the probability increases linearly from 0 to 1. Fischer & Marcy (1992) studied M dwarf binary systems and determined that, with a thermal eccentricity prior, the mean of the posterior of $a/r_{\rm proj} = 1.26$. We are able to reproduce this result with the same eccentricity distribution and a uniform prior on semi-major axis.

The priors on semi-major axis and orbital eccentricity both significantly affect the width of the posterior. The most optimistic priors (e = 0 and log-uniform a) result in an asymmetric 1σ interval spanning 0.29 AU. The most pessimistic priors (uniform e and a) produce a 1σ interval spanning 1.04 AU. The most realistic case (beta-distributed e and log-uniform a) results in a 1σ interval spanning 0.67 AU; dividing this interval by 2 yields the left-most point in Figure 2.4.

Precise astrometry can be taken to mean $\sigma_{\rm astro}$ is much smaller than the intrinsic ranges shown in Figure 2.3. We therefore expect that for measurement uncertainties less than 0.3 AU, these distributions will not be much affected and the

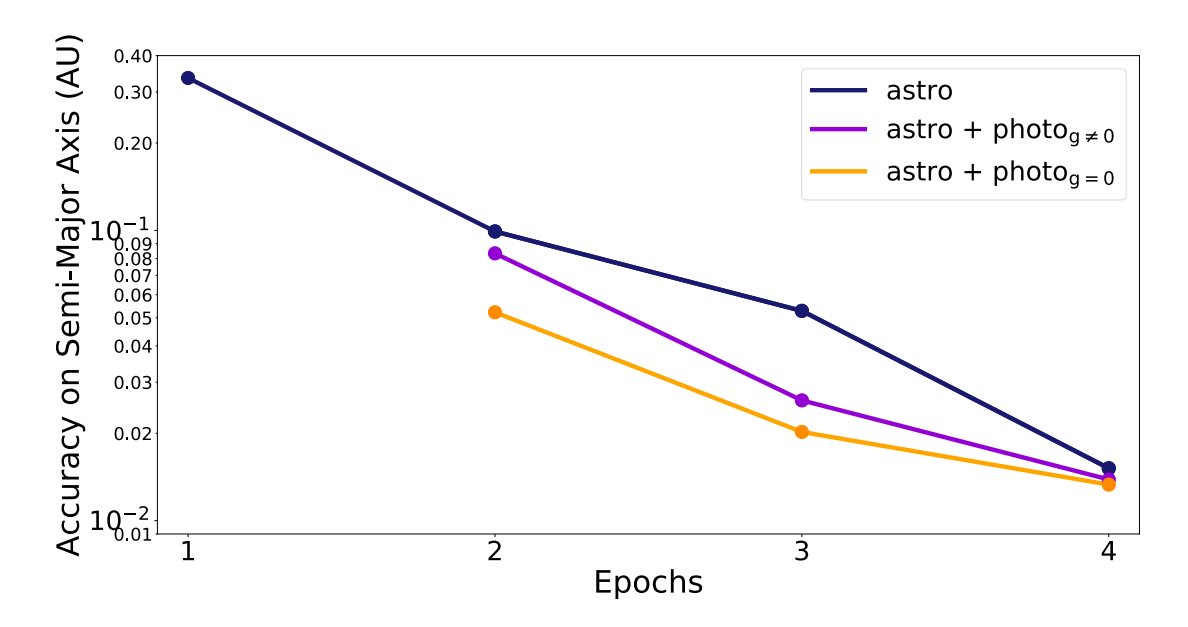


Figure 2.4: The 68% confidence interval (σ_{Δ}) on the accuracy of the semi-major axis for 100 runs at 1, 2, 3, and 4 detections. The blue line indicates these values for a model that only includes astrometry. The σ_{δ} for 1 epoch is taken from the the top-center panel of Figure 2.3. The yellow line is for a model including astrometry and photometry, where the phase curve is Lambertian and we presume to know this in our retrieval. The purple line also indicates a model with photometry, but where the generated planets have a Henyey-Greenstein phase curve, and the scattering parameter g is part of the fit. Models with astrometry + photometry provide better accuracy, particularly when the phase curve is Lambertian. Models with more epochs also yield improved accuracy, as expected.

posterior distribution is approximately independent of the astrometric uncertainty. But for three or more epochs, the accuracy of the retrieved semi-major axis will be approximately proportional to the astrometric uncertainty.

2.3.2 Orbit retrievals for 2, 3, and 4 epochs

For two or more epochs of direct imaging, photometry can play a useful role in constraining the orbit of a planet. Figure 2.4 compares the accuracy of semi-major axis retrievals, σ_{Δ} , for 2, 3, and 4 epochs. There is minimal improvement in the accuracy between 3 and 4 epochs, which is to be expected due to the number of data and parameters (Guimond & Cowan 2019): once the retrieval problem becomes over-determined, it is an optimization problem and we expect accuracy to improve as $N^{-\frac{1}{2}}$. We focus primarily on retrievals based on 2 or 3 epochs since these are cases where photometry significantly impacts retrieval accuracy.

At 2 epochs, all models constrain the retrieved semi-major axis to within 10%, where there is minimal improvement with the addition of a Henyey-Greenstein phase curve. Retrievals using a Lambertian phase curve brings retrievals close to within 5%. Notably, this is comparable to using 3 epochs of only astrometric data. At 3 epochs, using either a Lambertian or Henyey-Greenstein phase curve provides significant improvement and constrains results within 5%.

Figure 2.5 compares the accuracy of retrieved semi-major axis (σ_{Δ}) as a function of measurement uncertanties for 2 and 3 epochs. Unsurprisingly, in both cases we see smaller (better) accuracy for retrievals using a Lambertian phase curve compared to retrievals done with no photometric information, or those using a Henyey-Greenstein phase function. We also see better accuracy in all three retrieval scenarios with 3 epochs versus 2, as expected. When the uncertainties on astrometry and photometry are larger and the planet is only detected twice, the accuracy is slightly worse than if no photometric information was included at all. Additionally, with 2 epochs of data and a Henyey-Greenstein phase function, σ_{Δ} is found to have a stronger dependence on the photometric uncertainty, given that the slope of the contours are steeper.

We examine the effects of added photometric information on all Keplerian parameters in Figure 2.6 and Table 2.2. We find that photometric information always improves parameter retrieval results with the exception of Ω and M_o for retrievals done with 2 epochs. This is expected since these two parameters do not influence planet phase curves.

While a and e are intrinsic to the planet's orbit, the other parameters are dependent on the observer's position. Retrievals of a and e are always most improved

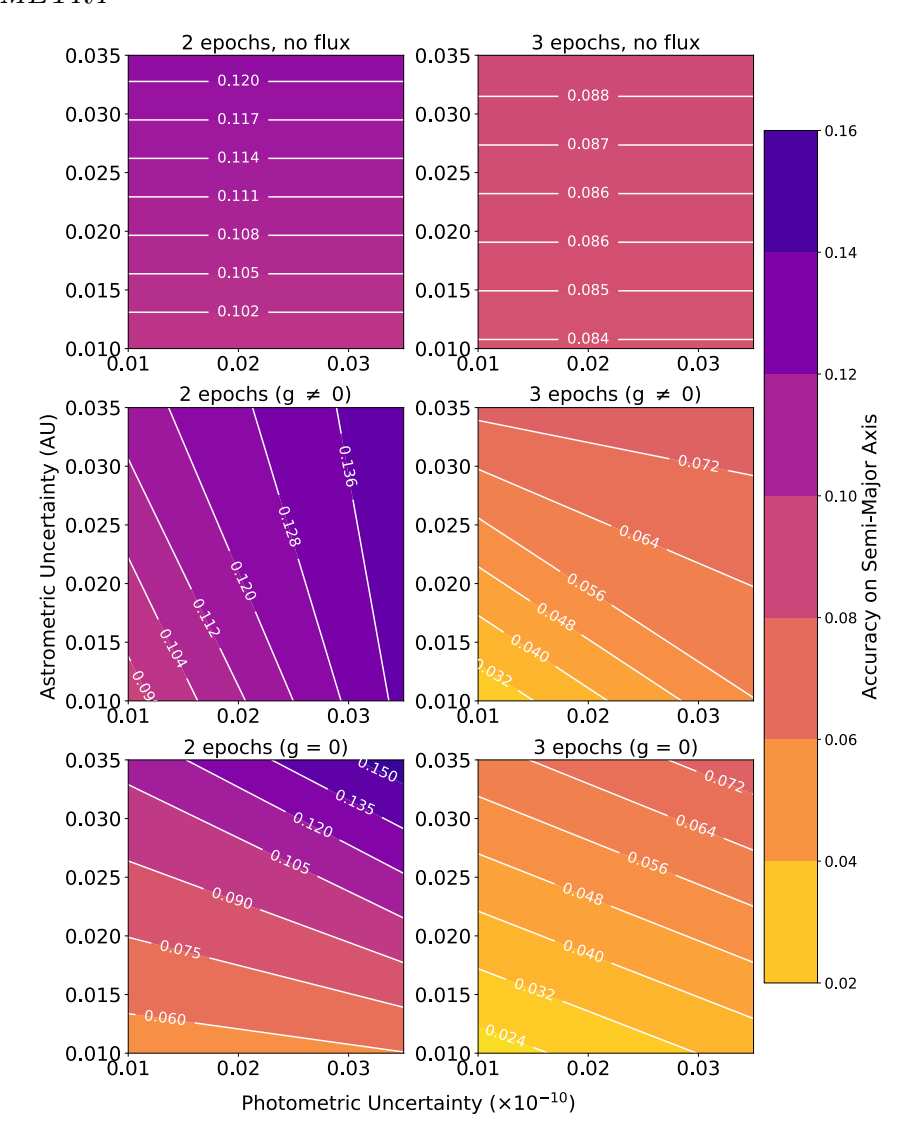


Figure 2.5: The accuracy of retrieved semi-major axis as a function of astrometric and photometric measurement uncertainty. Contour plots indicate the 68% confidence interval for 100 retrieved semi-major axis values $(\sigma_{\Delta a})$ determined for varying uncertainty values on photometry and astrometry of the synthetic data, for values of 0.01 and 0.035 AU for astrometry, and 10^{-12} and 3.5×10^{-12} . The left panels correspond to retrievals done for 2 epochs, and the right for retrievals done with 3 epochs. The top two panels indicate results for retrievals done with only astrometry (hence the constant values over increased photometric uncertainty). The middle two panels demonstrate results for retrievals done with astrometric + photometric information with a Henyey-Greenstein phase function, and the bottom two for a Lambertian phase function. Measurement uncertainty on astrometry impacts accuracy results more significantly than photometric uncertainty, except for 2 epochs of data with a Henyey-Greenstein phase function. With only 2 epochs of data, higher uncertainties on astrometry and photometry can provide worse accuracy than if no photometry is used. 29

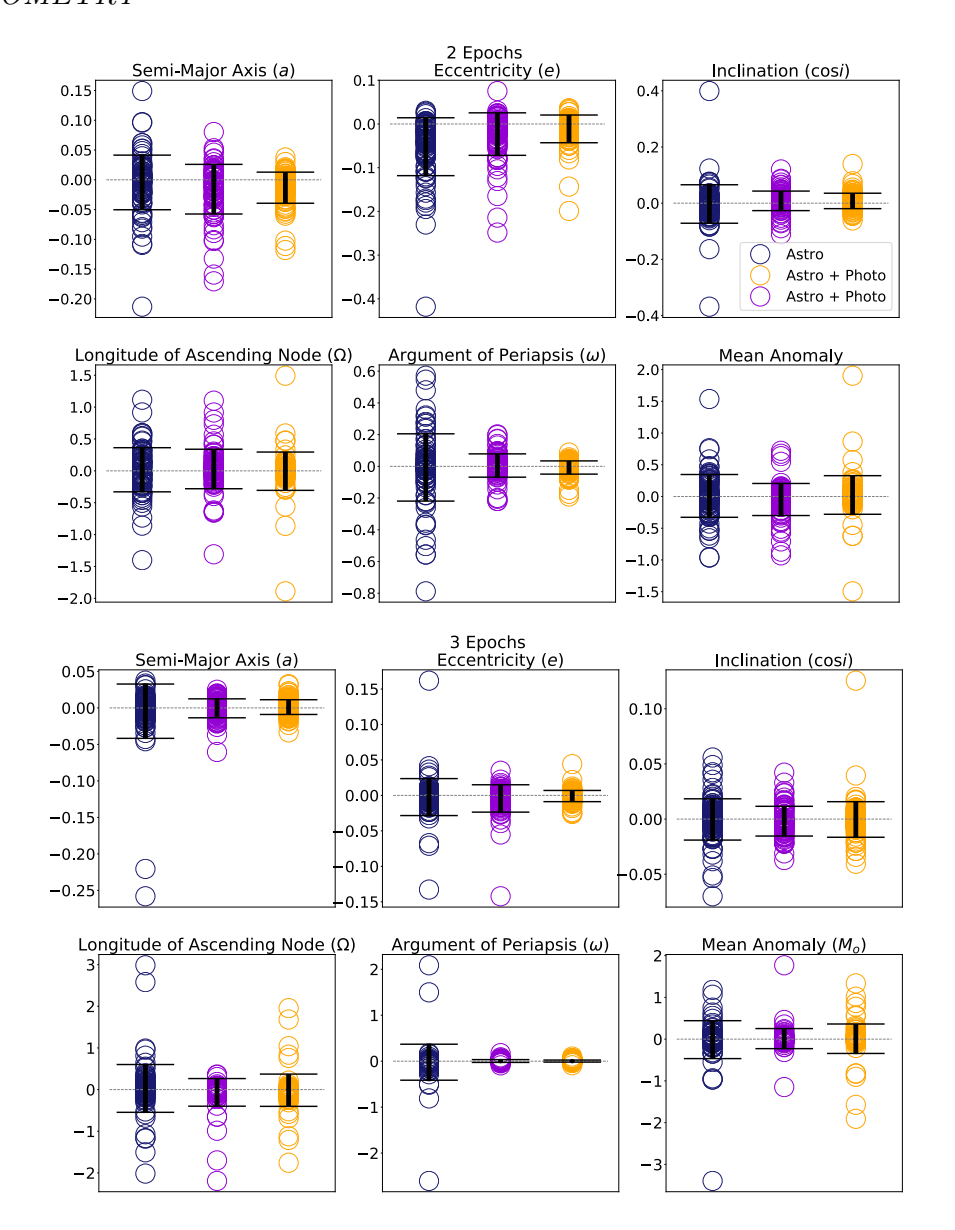


Figure 2.6: Accuracy of retrieved Keplerian parameters for two (top) and three (bottom) epochs of direct imaging 90 days apart. Each data point is the difference between the true parameter value and the one retrieved (Δ) and the error bars indicate the 68% confidence interval on these results for 100 planets (σ_{Δ}). Each panel corresponds to the retrievals performed for different Keplerian parameters. We demonstrate results for retrievals with astrometry (blue), astrometry + photometry with a Henyey-Greenstein phase curve (purple), and ones with astrometry + photometry with a Lambertian phase curve (yellow). These figures indicate that retrievals for the argument of periapsis (ω) benefit most from added photometric information, followed by semi-major axis (a) and eccentricity (e). Retrievals for the longitude of ascending node (Ω) and the mean anomaly (M_{o}) benefit the least.

 $CHAPTER\ 2.\quad ORBIT\ RETRIEVAL\ USING\ PLANETARY\ ASTROMETRY\\ PHOTOMETRY$

Parameter	Epochs		$\langle \Delta angle_L$	σ_{Δ_L}	$\langle \Delta \rangle_{HG}$	$\sigma_{\Delta_{HG}}$
	2	astro	-0.004	0.04		
		astro + photo	-0.01	0.03	-0.02	0.04
	3	astro	-0.004	0.04		
a		astro + photo	0.001	0.01	-0.0005	0.01
	4	astro	0.002	0.01		
		astro + photo	0.0001	0.007	0.0004	0.007
	2	astro	-0.05	0.07		
		astro + photo	-0.01	0.03	-0.02	0.05
	3	astro	-0.002	0.03		
<i>e</i>		astro + photo	-0.001	0.006	-0.004	0.02
	4	astro	-0.001	0.008		
		astro + photo	-0.0006	0.004	-0.0009	0.006
$\cos i$	2	astro	-0.003	0.07		
		astro + photo	0.008	0.03	0.008	0.03
	3	astro	-0.0003	0.02		
		astro + photo	-0.0009	0.01	-0.002	0.01
	4	astro	-0.001	0.009		
		astro + photo	-0.000006	0.007	0.0008	0.007
ω	2	astro	-0.007	0.2		
		astro + photo	-0.007	0.04	0.005	0.07
	3	astro	-0.02	0.4		
		astro + photo	0.0007	0.02	0.004	0.03
	4	astro	-0.007	0.07		
		astro + photo	0.0004	0.01	-0.02	0.2
	2	astro	0.02	0.3		
Ω		astro + photo	-0.005	0.3	0.03	0.3
	3	astro	0.03	0.6		
		astro + photo	0.006	0.4	-0.07	0.3
	4	astro	0.05	0.3		
		astro + photo	0.01	0.2	0.03	0.3
	2	astro	0.009	0.4		
		astro + photo	0.02	0.3	-0.05	0.2
	3	astro	-0.01	0.4		
M_o		astro + photo	-0.008	0.3	0.01	0.2
	4	astro	-0.03	0.2		
		astro + photo	-0.016	0.25	-0.01	0.2

Table 2.2: Bias, $\langle \Delta \rangle$, and accuracy, σ_{Δ} , for 6 Keplerian parameters. The true Keplerian values for each planet are randomly generated following the input distributions outlined in Table 2.1 in §2.2.2. These values are indicated for models with only astrometry, and then for models with astrometry + photometry with either a Lambertian or Henyey-Greenstein phase curve. These results are repeated for planets imaged at 2, 3, and 4 epochs.

when the phase curve of the planet is Lambertian, and when it has been detected 3 times. Photometric information most significantly improves ω , which makes sense as it describes the point of closest approach to the host star relative to its ascending node. It follows that information on a planet's changing brightness would significantly improve this parameter over simply using astrometric information.

2.4 Discussion

2.4.1 Caveats

We have assumed that the only constraints available are planetary astrometry and photometry. If directly-imaged planets are discovered and their orbits retrieved via stellar astrometry, then our results do not apply and are of merely academic interest (Meunier & Lagrange 2022). Likewise, if the orbits are first characterized via stellar radial velocity (Li et al. 2021), then the only parameter left to constrain is Ω , which is immune to photometric constraints.

By neglecting non-detections we have made the orbit retrieval problem somewhat easier: Guimond & Cowan (2019) noted that a non-detection epoch provides less than half the astrometric information as a detection epoch, and there is no photometric information whatsoever. On the other hand, by limiting out analysis to planets that are detected at all epochs, we have biased ourselves in favour of planets on face-on orbits, for which phase variations are more muted. We don't expect either of these biases to significantly impact our results because non-detections are relatively rare: 90% of our synthetic single-epoch observations result in a detection, and 85% result in detections at two epochs.

In our numerical experiment we assume that the imaged planets are alone in their star system. The presence of other planets could change whether additional photometry improves results. If another planet is imaged while the target is within the IWA, its photometry could lead us astray.

We also assume that images of a planet will be taken at fixed intervals of 90 days from the first epoch, which Guimond & Cowan (2019) demonstrate to be near-optimal if the planet has an orbital period similar to Earth's. Depending on our knowledge of the phase curve a priori this may not be the case. Rather, it could be preferable to image a planet at times where the brightness has changed most significantly.

2.4.2 Summary

Our results demonstrate a clear improvement in the retrieval of exoplanetary orbits given additional photometric information. We focused on the accuracy and precision of the retrieved semi-major axis since it is an intrinsic property of the orbit and first-order determinant of a planet's climate.

We showed that if the scattering phase functions of exoplanets can be predicted a priori, then photometry provides a 50% improvement in the efficiency of astrometric orbit retrieval: it takes three epochs of astrometry to constrain a planet's semi-major axis to 5%, whereas the combination of astrometry and photometry achieves the same accuracy in only two epochs. For comparison, a single epoch of astrometry, combined with reasonable priors, constrains the semi-major axis to approximately 30%.

If, on the other hand, we presume no prior knowledge of the scattering parameter g, then photometry only improves the two-epoch accuracy by $\sim 10\%$ but improves the three-epoch accuracy by a factor of 2. With four or more epochs of astrometry, the use of photometry only improves the retrievals by a few percent.

These results could indicate significant time and cost reduction for future direct imaging missions operating in visible light, such as HabEx or LUVOIR. We present a strong argument for the use of this additional photometric information if these missions anticipate operating with as few detections as possible. Constraining orbits more accurately and efficiently can improve estimates as to whether a planet is habitable, and whether it should be revisited for detailed characterization.

Our fiducial case assumes precise astrometry and photometry. Larger uncertainties on either measurements reduce the benefits of photometry. We find that increasing photometric uncertainty has a less significant impact than increasing astrometric uncertainty. This indicates that in most cases any measurement of changing brightness could be beneficial to orbit retrievals.

2.4.3 Conclusions

We have focused on Earth-like exoplanets orbiting Sun-like stars because they are the metric by which future direct imaging missions are compared (Stark et al. 2014b; Stark et al. 2019; National Academies of Sciences 2021). However, the principles outlined here apply equally well to other exoplanets imaged in reflected light and may be useful for the Roman Space Telescope.

The improved efficiency of using photometry is most useful for starshades, which slew much slower than a telescope equipped with a coronagraph. Hence a direct-imaging survey with a starshade pays dearly for each additional epoch. Even for a coronagraphic direct imaging campaign, the settling time after a slew can be comparable to the integration times, so reducing the number of revisits before triage of targets will improve the mission efficiency.

Well-calibrated planetary photometry has uses beyond orbit determination. At the very least, three or more epochs of astrometry plus photometry begin to uniquely constrain the HG phase curve parameter, hence hinting at the nature of the scattering mechanism (Henyey & Greenstein 1941). The shape of the phase curve may also betray latitudinal albedo variations (Cowan et al. 2012). Multi-band photometry, even at only 2–3 epochs, would strongly constrain the scattering properties of the planet; simultaneous multi-band photometry is easiest to envision with a starshade.

Acknowledgments

This work was supported by the McGill Space Institute, TEPS CREATE and NSERC. We thank Ben Farr for his valuable help with kombine. We also thank fellow MEChA group members Lisa Dang, Samson Mercier, Alex Gass, and Taylor Bell for their help working through various hiccups along the way. We thank Chris Stark and Ell Bogat for useful conversations at a 2021 STSci Virtual Symposium.

Chapter 3

Conclusion

Of the numerous methods used to discover exoplanets, direct imaging is by far the most technologically challenging. But it has perhaps the most promising outlook. Future missions such as Roman, HabEx, and LUVOIR will be capable of directly imaging exoplanets in reflected visible light, and will become the best way to characterize Earth-like planets. Current ground-based direct imaging experiments capture inherent heat from planets by detecting them in infrared, leaving only two-dimensional positional information (astrometry) at our disposal for orbit retrieval. Guimond & Cowan (2019) demonstrated that at least three detections are required to properly constrain a planets orbit with astrometry alone. Reflected visible light results in phase-dependent photometry as the planet moves around its host star. The work outlined in this thesis explores exoplanet orbit retrieval when photometry, in addition to astrometry, is included in our analysis.

This work focuses on retrieving the semi-major axis since it is inherent to a planet's orbit and is most indicative of climate and potential habitability. Not only have we demonstrated that the addition of photometry improves both accuracy and precision on semi-major axis retrievals, we have also shown that orbit retrieval can be done with as few as two detections of a planet. Although this work is specific to Earth-twins, these findings are applicable to any type of planet.

The improvement to orbit retrieval shown in this thesis is relevant to the future missions outlined above. Our findings demonstrate how future missions can be more efficient by saving both time and money, and can indicate which planets should be revisited for more detailed characterization. For instance, LUVOIR and HabEx have planned lifetimes of about 10 years and are expected to cost roughly 10 billion dollars. Per day this is 1 billion/365 days ~ 2.7 million. If it takes the telescopes 1 day to stabilize, and 1 day for exposure on the system, then each direct image will

CHAPTER 3. CONCLUSION

 $\cos t \sim 5.4$ million dollars. HabEx and LUVOIR plan to image about 50 planetary systems (Gaudi et al. 2020; The LUVOIR Team 2019a). If each one is characterized with one fewer direct image, then 270 million dollars would be saved.

There are many avenues of research related to this work that would be interesting to explore. For instance, we have begun work to determine when it is optimal to revisit a planet a second time, based on data garnered from the first epoch. We simulate a single direct image for newly discovered Earth-twins and sample a statistical distribution of orbits to determine where they are the least constrained. Strategic planning of follow up observations can significantly improve the quality of data acquired and the time it takes to computationally analyze it.

There are many other ways to significantly improve the direct imaging prospects of future missions. For instance, determining how to disentangle direct images from multi-planet systems would help to avoid confusion during characterization. The starshade design proposed by the HabEx team would allow for visible light direct imaging in multiple bands Gaudi et al. (2020). From this, it could be fruitful to determine how we might distinguishing different planets using colour information. It could also be worthwhile to examine how machine learning could improve accuracy and precision of orbit retrievals and planet characterization, and streamline the data analysis process of direct imaging experiments.

References

Beuzit, J.-L., Vigan, A., Mouillet, D., et al. 2019, Astronomy & Astrophysics, 631, A155

Bixel, A., & Apai, D. 2020, AJ, 159, 3

Blunt, S., Nielsen, E. L., Rosa, R. J. D., et al. 2017, The Astronomical Journal, 153, 229

Bowens, R., Meyer, M. R., Delacroix, C., et al. 2021, Astronomy & Astrophysics, 653, A8

Charbonneau, D., Noyes, R. W., Korzennik, S. G., et al. 1999, The Astrophysical Journal, 522, doi:10.1086/312234

Chauvin, G. 2018, Direct Imaging of Exoplanets at the Era of the Extremely Large Telescopes, doi:10.48550/ARXIV.1810.02031

Chauvin, G., Lagrange, A.-M., Dumas, C., et al. 2004, Astronomy & Astrophysics, 425, L29

Cowan, N. B., Abbot, D. S., & Voigt, A. 2012, The Astrophysical Journal, 752, L3

Crossfield, I. J. M. 2013, A&A, 551, A99

Currie, T. 2016, HR 8799: The Benchmark Directly-Imaged Planetary System, arXiv:1607.03980

Farr, B., & Farr, W. M. 2015, in prep

Fischer, D. A., Howard, A. W., Laughlin, G. P., et al. 2014, in Protostars and Planets VI (University of Arizona Press)

Fischer, D. A., & Marcy, G. W. 1992, ApJ, 396, 178

REFERENCES

Foreman-Mackey, D., Hogg, D. W., Lang, D., & Goodman, J. 2013a, Publications of the Astronomical Society of the Pacific, 125, 306–312

—. 2013b, Publications of the Astronomical Society of the Pacific, 125, 306

Galilei, G. 1610, Sidereus nuncius magna, longeque admirabilia spectacula pandens lunae facie, fixis innumeris, lacteo circulo, stellis nebulosis, ... Galileo Galileo: nuper a se reperti beneficio sunt observata in apprime vero in quatuor planetis circa Iovis stellam disparibus intervallis, atque periodis, celeritate mirabili circumvolutis ... atque Medicea sidera nuncupandos decrevit, doi:10.3931/e-rara-695

Gaudi, B. S., Seager, S., Mennesson, B., et al. 2020, The Habitable Exoplanet Observatory (HabEx) Mission Concept Study Final Report, arXiv:2001.06683

Gould, A., & Loeb, A. 1992, ApJ, 396, 104

Guimond, C. M., & Cowan, N. B. 2018, The Astronomical Journal, 155, 230

—. 2019, The Astronomical Journal, 157, 188

Henyey, L. C., & Greenstein, J. L. 1941, The Astrophysical Journal, 93, 70

Horning, A., Morgan, R., & Nielson, E. 2019, in Techniques and Instrumentation for Detection of Exoplanets IX, ed. S. B. Shaklan, Vol. 11117, International Society for Optics and Photonics (SPIE), 427 – 437

Kasdin, N. J., Bailey, V., Mennesson, B., et al. 2020a, in Space Telescopes and Instrumentation 2020: Optical, Infrared, and Millimeter Wave, ed. M. Lystrup, N. Batalha, E. C. Tong, N. Siegler, & M. D. Perrin (SPIE)

Kasdin, N. J., Bailey, V., Mennesson, B., et al. 2020b, Space Telescopes and Instrumentation 2020: Optical, Infrared, and Millimeter Wave, doi:10.1117/12.2562997

Kipping, D. M. 2013, Monthly Notices of the Royal Astronomical Society: Letters, 434, L51–L55

Konopacky, Q. M., Marois, C., Macintosh, B. A., et al. 2016a, The Astronomical Journal, 152, 28

—. 2016b, The Astronomical Journal, 152, 28

Kopparapu, R. K., Ramirez, R., Kasting, J. F., et al. 2013, The Astrophysical Journal, 765, 131

Lagrange, A.-M. 2014, Philosophical Transactions of the Royal Society A: Mathematical, Physical and Engineering Sciences, 372, 20130090

REFERENCES

Lagrange, A.-M., Gratadour, D., Chauvin, G., et al. 2008, Astronomy & Samp Astrophysics, 493, L21

Lagrange, A. M., Meunier, N., Rubini, P., et al. 2019, Nature Astronomy, 3, 1135

Lambert, J. H. .-. 1760, Lamberts Photometrie. (Photometria, sive De mensura et gradibus luminis, colorum et umbrae) (1760) (Leipzig: W. Engelmann)

Li, Y., Brandt, T. D., Brandt, G. M., et al. 2021, The Astronomical Journal, 162, 266

Macintosh, B. 2021, Direct imaging of giant exoplanets: an observers view (with attempted theory context)

Macintosh, B., Graham, J. R., Ingraham, P., et al. 2014, Proceedings of the National Academy of Sciences, 111, 12661

Macintosh, B., Graham, J. R., Barman, T., et al. 2015, Science, 350, 64

Macintosh, B., Graham, J. R., Barman, T., et al. 2015, Science, 350, 64

Marois, C., Macintosh, B., Barman, T., et al. 2008, Science, 322, 1348

Marois, C., Macintosh, B., Barman, T., et al. 2008a, Science, 322, 1348

—. 2008b, Science, 322, 1348

Marois, C., Zuckerman, B., Konopacky, Q. M., Macintosh, B., & Barman, T. 2010, Nature, 468, 1080

Marois, C., Zuckerman, B., Konopacky, Q. M., Macintosh, B., & Barman, T. 2010, Nature, 468, 1080

Meunier, N., & Lagrange, A.-M. 2022, A new estimation of astrometric exoplanet detection limits in the habitable zone around nearby stars, arXiv:2202.06301

Mordasini, C., Marleau, G.-D., & Molliè re, P. 2017, Astronomy & Astrophysics, 608, A72

Murray, C. D., & Correia, A. C. M. 2010, Keplerian Orbits and Dynamics of Exoplanets, ed. S. Seager, 15–23

NASA Exoplanet Science Institute Website. 2020, Planetary Systems Table

National Academies of Sciences, Engineering, M. 2021, Pathways to Discovery in Astronomy and Astrophysics for the 2020s (Washington, DC: The National Academies Press), doi:10.17226/26141

REFERENCES

Nielsen, E. L., Close, L. M., Biller, B. A., Masciadri, E., & Lenzen, R. 2008, The Astrophysical Journal, 674, 466–481

Oppenheimer, R. 2003, The Lyot Project: Coronagraphy

Pueyo, L., Soummer, R., Hoffmann, J., et al. 2015, The Astrophysical Journal, 803, 31

Quanz, S. P., Crossfield, I., Meyer, M. R., Schmalzl, E., & Held, J. 2014, International Journal of Astrobiology, 14, 279

Romero-Wolf, A., Bryden, G., Agnes, G., et al. 2021, Starshade Rendezvous: Exoplanet Orbit Constraints from Multi-Epoch Direct Imaging, arXiv:2101.01276

Russell, H. N. 1906, ApJ, 24, 1

Spiegelhalter, D., & Rice, K. 2009, Bayesian statistics

Stark, C. C., Roberge, A., Mandell, A., & Robinson, T. D. 2014a, ApJ, 795, 122

—. 2014b, ApJ, 795, 122

Stark, C. C., Belikov, R., Bolcar, M. R., et al. 2019, The ExoEarth Yield Landscape for Future Direct Imaging Space Telescopes, arXiv:1904.11988

Sudol, J. J., & Haghighipour, N. 2012, The Astrophysical Journal, 755, 38

The LUVOIR Team. 2019a, The LUVOIR Mission Concept Study Final Report, doi:10.48550/ARXIV.1912.06219

—. 2019b, arXiv e-prints, arXiv:1912.06219

Traub, W. A., & Oppenheimer, B. R. 2010, in Exoplanets, ed. S. Seager, 111–156

Wang, J. J., Graham, J. R., Dawson, R., et al. 2018a, The Astronomical Journal, 156, 192

—. 2018b, The Astronomical Journal, 156, 192

Wolszczan, A., & Frail, D. A. 1992, Nature, 355, 145

Zurlo, A., Vigan, A., Galicher, R., et al. 2016, Astronomy & Samp Astrophysics, 587, A57